Electrospun antibody-functionalized poly(dimethyl siloxane)-based meshes for improved T cell expansion

Alexander P Dang

Submitted in partial fulfillment of the
requirements for the degree of
Doctor of Philosophy
in the Graduate School of Arts and Sciences

COLUMBIA UNIVERSITY

2018

ABSTRACT

Electrospun antibody-functionalized poly(dimethyl siloxane)-based meshes for improved T cell expansion

Alexander P Dang

Adoptive cell transfer (ACT) has garnered significant interest in recent years within the medical field due to its potential in providing an effective form of personalized medicine for patients suffering from a wide range of chronic illnesses, including but not limited to cancer. By leveraging the patient's own cells as the therapeutic agent, concerns over patient compatibility and adverse reactions are significantly reduced. Central to this therapy is the ability to optimize cell quantity and cell activation in order to produce a more robust infusion to the patient.

This thesis focuses on two main aspects. The first is the materials synthesis and development of a novel platform for the *ex vivo* expansion of human T cells for ACT, while the second aims to elucidate the underlying structural mechanics of this platform. This platform, which consists of an electrospun mesh of micron and sub-micron diameter poly (dimethyl siloxane)-based fibers, aims to maintain the high surface-area to volume ratio characteristic of the current clinical gold standard. This also simultaneously allows for effective leveraging of T cell mechanosensing, a phenomenon previously discovered by our lab that is the ability of a human T cell to respond differently to surface mechanical cues. By modulating the concentration of poly (ε-caprolactone) in these fibers, a biocompatible polymer, the mesh mechanical rigidity was varied: this effectively allowed for the leverage of T cell mechanosensing by maintaining a low and tunable Young's modulus throughout. Additionally, safety concerns involving transfusion of the expansion platform

into the patient were addressed by having a single continuous substrate instead of an array of disjoint ferromagnetic beads.

Our results thus far indicate that this soft mesh platform can produce upwards of 5.6-12.5 times more T cells in healthy patients than the clinical gold standard while maintaining comparable levels of cellular activation and phenotypic distributions as measured through IFNγ secretion and expression of surface proteins CD107b, CD45RO, and CCR7, respectively. Additionally, this platform demonstrates the ability to produce improved expansion of exhausted (PD-1^{high}) T cells from CLL patients compared to the clinical gold standard across all analyzed Rai stages. Finally, experiments have shown our platform to be scalable to produce clinically relevant levels of cells (> 50 million) from a given starting population, thus indicating its potential in adaptation in larger scale *in vitro* systems. The currently demonstrated capabilities of our mesh platform thus hold significant promise in the clinical development and adoption of ACT, as well as the development of larger scale *in vitro* systems.

In order to elucidate the underlying structural mechanics of our platform, quantitative AFM studies have indicated a force-dependency in rigidity measurement, thus indicating that standard Hertzian contact models and their derivatives (DMT, Sneddon, etc.), may not be ideal in calculating the rigidity of this material. In order to better model the effective Young's modulus (E_{eff}) of the mesh and account for cantilever beam-bending type mechanical deformation, a modification of Euler-Bernoulli theory was established. This mathematical model was subsequently used to correlate fiber geometry parameters to bending stiffness, thus allowing for us to estimate E_{eff} for a range of meshes. Subsequent T cell expansions and comparison of data to previous expansions on planar surfaces provided verification of our model.

Table of Contents

List of Figures and Tables

Acknowledgements

The research performed in this report was made possible through funding support from the NSF GRFP, the Wallace Coulter Foundation, and the National Institutes of Health (R01AI110593). CLL patient cells were provided from the Dana Farber Cancer Institute at Harvard University through the diligent efforts of Dr. Jennifer R. Brown and Stacey Fernandes. Assistance in flow cytometry was provided by Dr. Siu-hong Ho and the flow cytometry core team at the Columbia Center for Translational Immunology, while assistance in AFM operation and instruction was provided by Dr. Tai-De Li at the City University of New York Advanced Science Research Center. Finally, electrospinning and preliminary SEM analysis was made possible through a collaboration with lab group of Dr. Helen Lu at Columbia University. The author would finally like to thank Dr. Lance Kam for five years of unyielding mentorship, without which this thesis would not have been possible.

Dedication

These past five years have been an amazing journey, filled with experiences that were nothing short of unforgettable, spanning distances all the way from New York to San Francisco to Hong Kong to Singapore. This thesis is therefore dedicated to all those who have made life that much more beautiful these past few years, but especially to Steffi Liu for her unendless support, years of insight and friendship, and impeccible taste in gin; to Christie Ho for her wit, sarcasm, love, and our endless hours of laughter; to Stephanie Lau for her ability to always brighten up a rainy day and her penchant for hedgehogs; to Celine Cua for her endless smile and love of garlic; to Wendy Mo for never failing to bring a smile to your face and brilliant mind; to Irene Kwok for the miles and miles of laughter and fun; and finally to Dr. Dorothy Wong, since as a medical doctor, she one day will likely be unclogging my arteries.

Introduction and Motivation

According to recent reports by the National Cancer Institute, cancer remains one of the leading causes of death in the United States, with approximately 16.5 million Americans currently diagnosed with some form of cancer, and an additional 1.5-2 million new cases projected for 2017 alone[1]. As such, cancer is currently projected to become the leading cause of death in the United States by 2024 and thus poses a significant burden to the current healthcare system. In spite of its extensive history of clinical use and relatively low cost, chemotherapy has significant drawbacks for both the patient and the physician due to its numerous side effects such as immunosuppression, chronic nausea, and damage to friendly tissue[2]. Bone marrow transplantations, while effective, likewise induce immunosuppression and furthermore present the physician with concerns involving donor-patient compatibility, donor availability, and tissue harvesting. Additionally, bone marrow transplantations invoke significant financial costs to both clinics and patients alike[1]. In recent years, more targeted therapies such as monoclonal antibody-based drugs have seen increased use in the clinic due to their ability to induce little to no significant damage to friendly tissue, while maintaining a high level of tumor cell targeting efficiency. However, high costs to both the clinic and the patient, as well as immunosuppression remain burdens to the physician and the patient[2]. Furthermore, patient compliance arises as a concern due to the requirement of multiple doses for full treatment[2]. Therefore, there currently exists an unmet clinical need for an effective form of cancer therapy that can simultaneously minimalize collateral damage to non-cancerous tissue and other side effects while being cost-effective.

To address these concerns, researchers have turned towards cell-based adoptive immunotherapy in recent years, a growing field that has shown recent successes towards the treatment of various chronic diseases, especially cancer[3]. Cellular therapy is rapidly developing as a powerful component of medicine, complementing the use of small-molecule and biologic agents. Adoptive cell transfer (ACT) of T lymphocytes for treatment of cancer is a prominent example of this emerging approach. Current implementations of ACT involve *ex vivo* expansion of a starting population of cells, producing clinically relevant numbers of these agents and also allowing manipulations that are not practical in vivo, most notably introduction of chimeric antigen receptors (CARs)[4]. In this therapy, a specific subset of the patient's own immune cells is removed from the body and cultured, or expanded, in an *ex vivo* environment whilst being stimulated against the target antigen. Further modification of cells, such as the introduction of a new T cell receptor (TCR) via a viral transduction, is also possible during this process. Upon reaching a target number of expanded cells, stimulated cells are isolated from the culture and ultimately re-introduced into the patient[3]. By leveraging the patient's own cells in order to fight the disease via targeting of a specific antigen, one effectively attains a high targeting level of cancerous cells, low adverse host-response, and can furthermore induce long-term immunity to the patient, thus significantly reducing the probability of remission[5]. Furthermore, currently existing technology can be readily adapted to support such therapies on a large scale, such as by the use of industrial-scale bioreactors and cell culture facilities. Full deployment of this type of ACT will require overcoming several challenges in cell manufacture, including technology scalability and minimization of the level of technical skill needed to carry out cellular expansions.

Although first described in detail by Rosenberg *et al* through their use of *ex vivo* expanded natural killer (NK) cells to treat metastatic melanoma in human subjects[6], current immuno-therapeutic treatments involve the use of other types of immune cells, such as T cells and dendritic cells (DCs). One particular application of interest currently is the use of T cells for treatment of both acute lymphoblastic leukemia (ALL) and chronic lymphocytic leukemia (CLL)[3, 7]. Other treatments include the use of DCs for prostate cancer therapy[7]. Given the wide range of current and potential applications of this field, adoptive immunotherapy presents researchers with promising solutions for oncological treatments and other chronic illness.

In current implementations, T lymphocytes are expanded in an *ex vivo* environment followed by transfusion into the patient, thus allowing for engineering of T cells with high target specificity and low levels of host response[3,5]. The usage of T cells as opposed to other types of cells (such as NK cells) is of particular advantage due to the ability for a subset to differentiate into effector memory and central memory T cells, thus promoting long-term immunity. Although there are a variety of platforms for T cell expansion including the ImmunoCult™ tetrameric antibody complexes by Stemcell Technologies and the nanobead-based T Cell Activation Kit by Miltenyi Biotec, in what is commonly accepted as the clinical gold standard, the *ex vivo* expansion of T cells is typically initiated by exposing isolated patient T cells to rigid polystyrene beads (Dynabeads®) of approximately 4 µm in diameter that present covalently attached activating antibodies, or agonists, to surface proteins CD3 and CD28, which together provide the primary and secondary activation signals for T cells respectively[3]. Cells are cultured on the Dynabead® platform for up to four days, after which beads are separated from expanded T cells in order to prevent overstimulation. This

is facilitated via the embedding of the beads with ferromagnetic cores, thus allowing for magnetic removal of beads prior to reintroduction of expanded cells into the patient[9].

However, Dynabead®-based treatment can be improved upon in three ways. First, it has been shown that post-bead separation, residual beads still remain in solution and stand a high risk of being introduced into the patient[10]. This unaddressed concern may potentially present future health complications to the patient. An additional improvement would be the increase of agonist-coated surface area-to-volume ratio, which can be made possible from the transition from a magnetic bead-based format to a three-dimensional fibrous mesh-based format. The use of 3D fibrous meshes is of particular advantage due to their pre-existing usage in tissue scaffolds, stemming from their ability to mimic the natural *in vivo* environment[11], or in the case of T cells, the cortical thymus[12,13]. Finally, recent experiments have indicated that T cells undergo mechanosensing via non-integrin-based and non-cadherin-based cell-substrate interactions[14]. Although the exact mechanism for this phenomenon has not yet been fully elucidated, it has been indicated that higher levels of cell proliferation of human T cells can be induced by culturing on a less rigid substrate, particularly surfaces with rigidities on the range of 100 kPa to 2-3 MPa. As the Dynabead® platform currently exhibits Young's moduli on the order of single digit GPa, a new softer platform may effectively improve current cell expansion capabilities through the leveraging of T cell mechanosensing. To summarize, it is hypothesized that by combining these three factors, one can fabricate a more robust and safer platform for T cell-based adoptive immunotherapy via electrospinning while maintaining or surpassing the cell expansion efficacy of the clinical gold standard.

Electrospinning offers a facile and cost-efficient method for the synthesis of aligned and unaligned polymeric fibers with uniform diameter ranging from several microns down to tens of nanometers[15, 16]. In this process, a solid polymer is dispersed in an organic solvent and is pumped at a fixed rate through a small orifice while being subjected to a very high electric potential towards a grounded collection electrode. As the liquid approaches the tip of the orifice, the liquid stream experiences three conflicting forces: electrostatic repulsion between particles due to the charging of the liquid pushing the jet apart, surface tension at the liquid-air interface holding the liquid jet together, and the aforementioned electric field, which drives the liquid jet towards the collection electrode. These forces ultimately stretch and pull the liquid jet towards the collection electrode at high speeds, thus causing the solvent to vaporize and forming a solid polymer fiber. Due to its scalability and ease of operation, electrospinning offers researchers unique advantages towards the synthesis of 3D fibrous meshes[15].

One successful platform for initiating expansion is the Dynabead® (ThermoFisher Scientific) system, which consists of microscale plastic beads that present on their surface activating antibodies to CD3 and CD28, two surface proteins on the T lymphocyte outer membrane that together promote functional activation and subsequent cell proliferation. The use of microbeads makes this approach highly scalable, making this platform appropriate from bench to clinical setting, and is readily compatible with current bioreactor technologies[9].

This thesis effectively introduces an improved platform for T cell expansion that brings together two concepts of biomaterials design. The first is the use of a fiber mesh as the activating substrate, which similarly to microbeads provides a large surface area to volume ratio for T cell activation. Importantly, this format offers simpler removal from the cell growth environment than the

Dynabeads platform; in that system, a magnetic field is used to collect the beads, but removal is often incomplete, and thus can pose potential, unstudied complications if subsequently introduced into the patient. The second concept captured in this new platform is the use of mechanical rigidity to enhance cell growth. The ability of cells to sense and respond to the mechanical properties of the extracellular environment has been largely established, predominantly in the context of cells interacting with extracellular matrix proteins through integrin receptors[17]. In subsequent studies by O'Connor *et al.*, it was demonstrated that T cell expansion also exhibits sensitivity to the mechanical rigidity of the activating material. In that study, anti-CD3 and anti-CD28 antibodies were attached to planar substrates of the Sylgard 184 formulation of poly (dimethyl siloxane) (PDMS)[18]. Reducing the ratio of cross-linker to elastomer base produced a change in bulk Young's modulus, decreasing it from the typical 2 MPa to the range of a few hundreds of kPa, but more importantly, increased the number of T cells produced in a single round of expansion by several fold. This was unexpected in that CD3, the T cell receptor (TCR) complex of which it is part, as well as CD28 have much weaker connections to the contractile cytoskeleton than do integrins and other transmembrane receptors normally associated with cellular mechanotransduction. This primary purpose of this report thus seeks to create a mechanically soft, mesh fiber platform for the purpose of improving expansion of T cells.

This platform was fabricated using electrospinning: a well-established, high-throughput technique in which a polymer in solvent is dispensed from a needle under a high electric potential towards a target. This balance of electrostatic forces and surface tension promotes formation of a well-controllable fiber geometry, which is captured in the final material[15]. This approach is well suited for producing fibers of micrometer to sub-micrometer diameters, and is well-suited for polymeric

solutions in which evaporation of a working solvent leads to solidification of the final material[16]. Although processing considerations such as the toxicity and commercial availability of the solvent should be taken into consideration for the commercial development of a clinically used platform, such factors will not be explored in this thesis.

PDMS is a biocompatible elastomer formed by the crosslinking of multiple siloxane-based backbones via shorter carbon-based linker units. As such, PDMS offers a facile method for the variation of surface rigidity through modulation of the crosslinker-to-base ratio. This variation allows for production of PDMS slabs with Young's moduli ranging from tens of kPa to hundreds of MPa. Furthermore, its current use in a wide range of applications, including various FDA-approved medical devices, as well as its commercial availability and low cost, make it an attractive material for the fabrication of substrates for cell stimulation[19].

Due its viscosity and immiscibility in most organic solvents however, electrospinning of pure PDMS fibers remains a challenge, regardless of grade and composition[20,21]. Notably, formation of a PDMS elastomer typically involves the catalyzed formation of crosslinks between long chains in a curing phase, rather than removal of a solvent. Therefore, the formation of well-defined PDMS nano or microfibers via electrospinning has to date been only reported in experiments where the PDMS pre-polymer is mixed with another polymer such as poly (vinyl pyrrolidone) (PVP) or poly (methyl methacrylate) (PMMA) in an organic solvent. Electrospinning of pure PDMS microfibers remains non-elucidated as of this writing[21].

An approach used in current experiments is to combine PDMS with poly(ε-caprolactone) (PCL), a biocompatible polymer that has been used extensively in electrospinning and other medical

devices[22], in the feed solution in order to allow for a more suitable viscosity and processing of the elastomer material. Because the bulk rigidity of PCL can vary anywhere from tens of MPa to single digit GPa[22], the addition of PCL to a PDMS material will inevitably make the overall Young's modulus higher than that of pure PDMS. Although a material with a low Young's modulus is desired for the current application, the addition of a more rigid viscosity-modulatory material may be essential for the formation of the material as a whole.

As T cell focal adhesions are on the scale of hundreds of nanometers[23], central to the notion of rigidity-based mechanosensing is what is the rigidity of the material on a very local scale: cell-material interactions will undoubtedly have a profound effect on the cell proliferation and activation. While standard uniaxial tensile testers readily provide facile measurements of bulk rigidities, these figures would not accurately reflect rigidities on a cellular level, again, due to the small length scales and geometries involved. Therefore, in order to probe substrate rigidities on the nanometer to micrometer scale, atomic force microscopy (AFM) presents itself as an ideal tool, in particular, its ability to probe nanometer-level mechanical properties of materials[22]. By detecting minute shifts in the deflection of the incident laser along with changes in voltage in the piezoelectric elements of the cantilever arm, a modern AFM can measure properties such as Young's modulus, tip adhesion, and tip deflection down to single digit Pa, pN, and nm, respectively[22].

Typical AFM measurements and rigidity calculations rely on underlying assumptions on the material itself. One of the most basic and time-trusted models for AFM contact measurements is the Hertzian contact model. In this model, the AFM tip is modeled as a hard, minute tip exerting a point force that does not experience any type of strain whatsoever as it comes in contact with the

material[24]. The Hertzian model further assumes that the substrate is a semi-infinite plane, the deformation of the material is purely elastic, and that local warping around the point of contact of the material does not occur, i.e., work hardening is negligible. In this model, the force applied by the AFM scales inversely with the Poisson's ratio of the sample and linearly with the sample Young's modulus[24]:

$$F = \left(\frac{4\sqrt{r}\delta^{3/2}}{3}\right)\frac{E}{(1-\nu^2)}$$

In this equation, r represents the AFM tip radius, δ is the depth of the indentation, E and ν represent the Young's modulus and Poisson's ratio of the sample, respectively, and F represents the force exerted by the tip downwards onto the sample. Terms on the left thus correspond to properties of the indentation while indenter while terms on the right correspond to sample mechanical properties. While this model inevitably has its flaws (local deformation of a material will always occur, tips will exhibit at least some van Der Waals forces-based adhesion to the material, etc.), it nonetheless provides a reasonable figure for the rigidity of bulk materials.

Various models have sought to improve on the Hertzian contact model and are thus more prominently used in modern AFMs. One such model proposed by Derjaguin, Muller, and Toporov, colloquially known as the DMT model, assumes a basic Hertzian interaction between the tip and substrate, but factors in forces of attraction outside the circular tip contact area[25]. Another common model by Sneddon has also seen common use in AFM, in which the indenting tip is modeled as a cone with half angle α.

$$F = \left(\frac{2\delta^2 \tan\alpha}{\pi}\right)\frac{E}{(1-\nu^2)}$$

In this model, the applied AFM force F is seen to scale proportionally with the square of the indentation depth, although the contribution from the sample itself remains constant. It should be noted however that one key fundamental assumption for both the DMT and Sneddon models is that the material is a semi-infinite plane[24,25]. It should be noted that AFM manufacturers typically apply their own proprietary modifications of these models in the calculation of surface rigidity in order to account for a wide range of factors, such as static electricity, magnetic moments, minute changes in tip resonant frequency, etc[25].

If one was to use a standard sharp conical AFM tip with diameters under 50 nm, neither of these three contact models would likely be the most accurate for measuring the rigidities of fibrous meshes with diameters on the order of single microns. One reason for this is readily apparent: mesh fibers cannot be accurately approximated as semi-infinite planes. If one was to imagine a single mesh fiber as a simply supported cylindrical beam subjected to a single point force (no adhesive forces between the beam and the support), one could imagine a rudimentary model for the interaction between a sharp conical AFM tip and mesh fiber as described below (see fig. 1).

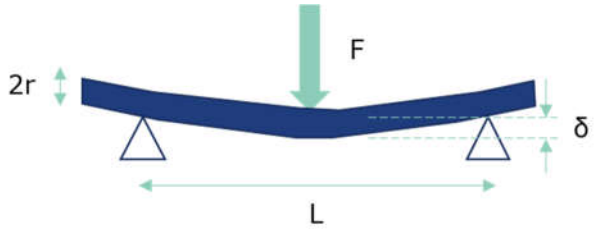

Figure 1: Standard beam bending model for a single mesh fiber with effective length L, radius r, and bulk modulus E supported by two simple (horn) supports

According to unidimensional cantilever mechanics, the maximum deflection of the beam δ in this case can be readily calculated as the following, where I represents the second moment of inertia of the beam, assumed here to be cylindrical[26].

$$\delta = \frac{FL^3}{48EI} \qquad I = \frac{\pi r^4}{4}$$

A back-of-the-envelope calculation with mesh parameters, herein approximated as 10^{-6} m, 10^{6} Pa, 10^{-9} N, and 10^{-5} m for r, E, F, and L, respectively, reveals that δ would be on the order of tens to several hundreds of nanometers. As mesh fibers would ideally have dimeters in the range of single digit microns, a deflection of up to several hundred microns would undoubtedly have non-negligible skew on rigidity measurements. Furthermore, tip adhesion and local deformation of the material become non-negligible factors as unlike metals and ceramics, PDMS is an inherently viscous and soft material.

Therefore, the goal of this thesis is to identify parameters of the final mesh material that can optimally promote T cell activation and expansion, as well as to delve into the mechanics of how fiber geometry can affect human T cell mechanosensing. Specifically, this thesis project will strive towards the construction of a mathematical model for the perceived rigidity of a fiber as a function of fiber parameters, and furthermore seek to verify such a model via a cell-based mechanosensing study.

T cell activation and phenotype

The activation of $CD3^+$ T cells in the body is a key aspect of the adaptive immune system, assisting the body in developing a targeted response to a specific set of antigenic markers. Activated conventional T cells can be generally divided into $CD4^+$ and $CD8^+$ subtypes (often termed helper T cells and cytotoxic T lymphocytes, respectively)[13]. The former is generally involved in enhancing antibody production from B cells and secreting vital cytokines to further activate the adaptive immune system, whereas the latter typically seeks out and terminates infected host cells, tumor cells, and bodies expressing non-host antigens through association with their major histocompatibility complex I molecules (MHC-I)[13]. These cells are therefore most commonly associated with implant and transfusion rejection, although there have been studies showing that certain helper T cells occasionally express CD8 and likewise, certain cytotoxic T lymphocytes occasionally express CD4. In addition to these two main types, regulatory T cells (T_{reg}s) suppress the function of both $CD4^+$ and $CD8^+$ T cells. Naïve T cells, which are formed in the medullary and cortical thymus, get activated through two independent signaling steps in the body to ensure that premature activation or over-activation does not occur. The first signal occurs through the antigen-specific T cell receptor (TCR), and causes signal propagation through surface protein CD3, in particular, the ε-subunit. This primary stimulatory signal occurs in the body through an antigen presenting cell (APC), most commonly a macrophage or dendritic cell through binding with the major histocompatibility complex II (MHC-II) that has already been loaded with target antigen. Following the primary stimulatory signal, secondary stimulation signal comes via surface protein

CD28. This activation signal comes from binding with CD19 on a so-called licensed B cell expressing CD80 or CD86. Both signals are required for T cells to transition from naïve T cells to activated T cells: those that only receive TCR signaling but not any other co-stimulatory signal leads to the formation of anergic T cells, while naïve T cells that bind to friendly host antigen undergo apoptosis to prevent autoimmune attacks[13].

Although multiple classification schemes exist for activated T cells, these cells are generally divided into three separate subcategories. Effector T cells broadly encompass most of the cytotoxic T lymphocytes as well as helper T cells and T_{reg}s that are formed during the adaptive immune response. These cells, most of which will undergo apoptosis after the target or invading body has been removed, typically express CD44 and CD45RA, but not CD62L or CCR7 (also known as CD197). Effector memory T cells on the other hand are long-lived T cells that will circulate in the peripheral blood after the immune response has died down, and are designed to amplify the initial immune response should the same antigen or set of antigens present themselves in the body again. These cells typically express CD45RO (a truncated form of CD45RA and a typical marker for memory cells), but do not express CCR7 or CD62L since they do not have the need to further migrate to the periphery. Finally, central memory T cells are functionally similar to effector memory cells, but primarily reside in the lymph nodes and central blood, although they may migrate out into the periphery. These cells express both CCR7 and CD62L, as well as CD45RO. Due to the different surface marker expression of these cell types, performing flow cytometry with stains for CCR7 and CD45RO can gate a mixed T cell population into effector, effector memory, central memory, and naïve T cell sub-populations[13].

The current model for *ex vivo* cell expansions typically involves sending patient cells from the clinic to an external facility for processing. Following activation and proliferation, the final cell product needs to be transported back to the clinic for infusion into the patient[27]. Although this isolation, growing, and transfusion process may need occur more than once for any given patient, one constant factor is the relatively high cost for purchasing and maintaining the bioreactor systems required for this expansion process, in addition to paying technicians and bioreactor operators. Although the need for a technology to optimize cell number is readily apparent, the demands of the patient naturally gives rise to the question of what phenotypic distribution is optimal. When the final cell product is transfused back into the patient, these cells will have seen target antigen for the second time. That is, cells will be undergoing secondary stimulation, or restimulation, instead of the primary stimulation in the bioreactor environment. Therefore, for the purposes of adoptive immunotherapy, a higher percentage of both effector memory and central memory cells would be optimal for the patient, as these cells can readily stimulate a response to target antigen, self-replicate, and / or differentiate into effector cells. It is postulated that an infusion with a higher percentage of effector cells but a lower percentage of effector memory and central memory cells will not trigger as strong of a response due to the short-lived nature of effector cells without the presence of target antigen[27].

T cell mechanosensing

It has been previously determined that many types of cells in the human body ranging from chondrocytes[28] to neurons[28] sense and respond to mechanical forces via focal adhesions, typically through integrin-based and cadherin-based interactions[26]. Such interactions with the extracellular environment via mechanosensing are critical in order for individual cells to move locally, regulate

self-repair, and undergo differentiation[28]. Under normal physiological conditions, the activation of naïve T cells occurs in the thymus through the recognition of a target antigen presented via DCs. In the first part of activation, naïve T cells are engaged via the T cell receptor (TCR) through interaction with a target antigen-coupled type II major histocompatibility complex (MHC-II) and the subsequent formation of the immune synapse. This initial stimulation subsequently allows for co-stimulation via CD28 on the surface of the T cell thorough coupling with CD19 on the surface of a B cell[15, 16, 18] and the prevention of apoptosis for the naïve T cell. Therefore, it should be noted that both stimulation via the TCR and co-stimulation via CD28 are necessary for T cell activation. Although it has been previously established that T cells do not undergo mechanosensing via integrin-based receptors, the exact signaling mechanism by which T cells translate mechanical cues into cellular events is currently not fully understood.

Initial experiments in this field performed by Judokusumo *et al*[12] to demonstrate that T cells in fact undergo mechanosensing focused on expression levels of interleukin-2 (IL-2), a cytokine involved in immune responses[16], in addition to expression levels and patterns of zeta-chain associated protein kinase 70 kDa (ZAP-70) and Src family kinase proteins (SFK) around the immune synaptic region as a function of substrate rigidity. The evaluation of ZAP-70 and SFK was of particular importance due to their previously known role in signal transmission and transduction in T cells. For this experiment, isolated mouse $CD4^+$ cells were cultured on poly(acrylamide) gels of rigidities at either 10, 25, 100 or 200 kPa coated with anti-CD3 and anti-CD28 antibodies. Results indicated that for substrates with Young's moduli below 25 kPa, IL-2 secretion levels decreased with decreasing rigidities, while there was a positive but saturating correlation between IL-2 levels and substrate rigidity. Furthermore, their results indicated that while stiffer substrates all exhibited

increased cell adhesion, there again was a saturating effect. Analysis of the presence of ZAP-70 and SFK via confocal microscopy revealed a similar pattern in which cells cultured on substrates with Young's moduli equal to or above 25 kPa exhibited higher levels of ZAP-70 and SFK than the softer 10 kPa substrate, thus fostering the notion that for substrates with rigidities below a certain threshold, T cell mechanosensing fundamentally behaves differently.

While the experiment performed by Judokusumo *et al.* provided a suitable framework for future T cell mechanosensing studies, this experiment did not offer significant insight into the behavior of non-murine T cells. In order to address this knowledge gap, this experiment was subsequently expanded upon by O'Connor *et al*.[18] through their usage of human $CD4^+$ and $CD8^+$ cells in order to further establish an optimal range of substrate rigidities for T cell stimulation. In this experiment, planar slabs of poly (dimethyl siloxane) (PDMS) of Young's moduli ranging from 50-100 kPa to approximately 2.3 MPa were fabricated by modulating the ratio of PDMS base to crosslinker ratio. Substrates were then functionalized with anti-CD3 (OKT3) and anti-CD28 (clone 9.3) antibodies and ultimately used to culture isolated $CD4^+$ / $CD8^+$ human T cells. In order to measure T cell activation, researchers focused on cell counts (population doublings) over the course of up to 14 days and IL-2 expression levels over the course of 72 hours. Results for cells cultured on PDMS surfaces were subsequently compared against human T cells cultured on anti-CD3 and anti-CD28-coated microbeads of approx. 4.5 μm diameter.

The data from this study indicated that there was a correlation between lower substrate Young's moduli and higher IL-2 secretion levels as well as population doublings. Specifically, it was observed that an approximate four-fold increase in overall culture yield was obtained by transitioning from the stiffest PDMS substrate (1:5 ratio of dimethyl siloxane monomer to base)

to the softest PDMS substrate (1:50 ratio of crosslinker to base) as seen in figure 2A of their paper. Researchers attributed this to more prolonged blast phase induced on cells cultured on the softer substrates due to cell volume data, as seen in figure 2C. It should be noted that for this experiment, an average cell volume of over 400 fL was considered to be blasting. This notion was further supported by carboxyfluorescein succinimidyl ester (CSFE) assays in conjunction with flow cytometry to track cell divisions and generations, as seen in figure 2E of their paper. Here, it was observed that cells cultured on planar substrates with softer rigidities underwent more divisions than cells cultured on stiffer substrates, especially with concentrations of IgG capture antibody below 1 µg / mL at 72 hours' post-stimulation. Likewise, cells cultured on the softest planar substrates exhibited approximately 3 times as much IL-2 as cells cultured on the stiffest planar substrates as measured by quantitative real-time PCR. However as seen in figure 2D of their paper, it was noted that this phenomenon was not the same for microbeads, with all rigidities yielding approximately equal levels of interleukin-2 (IL-2). These results therefore indicate that substrate mechanical properties, substrate morphology, and antibody presentation are all potentially key variables in controlling the activation and proliferation of human T cells.

Electrospinning and the use of electrospun micro- and nanofibers for cell culture and tissue engineering

The usage and development of electrospun fibers of micron and sub-micron diameters has been previously widely reported in the literature, with applications ranging from drug delivery to tissue engineering. First developed and patented by James Cooley in 1934, electrospinning has gained significant traction in recent years due to its ability to produce biomaterials and biomedical

products such as polymeric fibers and mats with controllable physical and chemical properties in a high-throughput and cost-efficient manner.

In electrospinning, a spinning solution consisting of a polymer uniformly dispersed in a volatile solvent is pushed slowly towards a grounded collection electrode at high electric potentials, typically in the kV range (see figure 2).

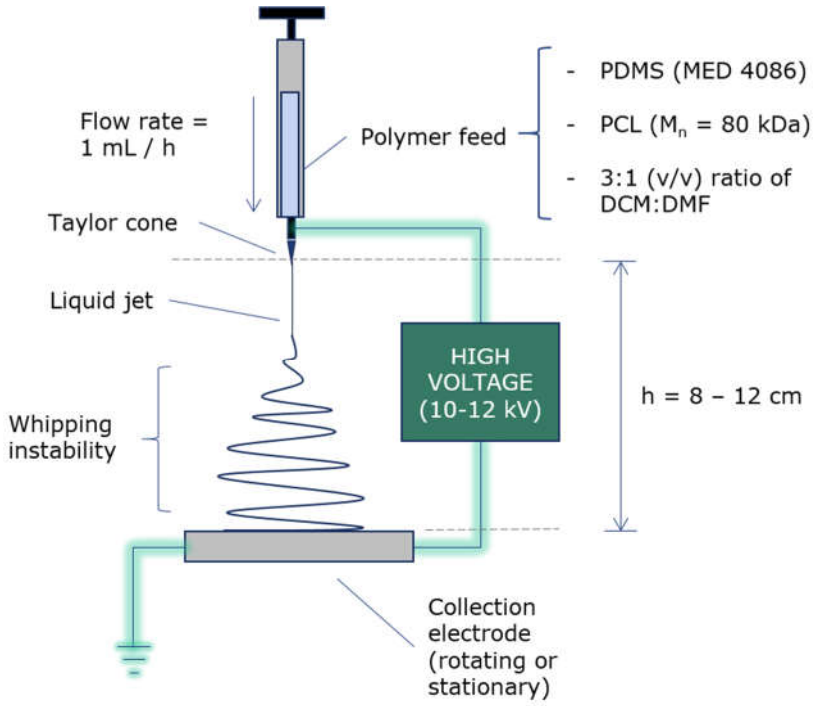

Figure 2: Basic electrospinning setup showing one potential polymeric feed formulation

As the highly charged polymer approaches the tip of discharging device, which is typically a blunted and sanded needle, the polymeric solution experiences a combination of two forces: the electrostatic repulsion between individual molecules in the spinning feed, driven by the charging of the fluid, and the intermolecular forces of attraction between those same molecules and surface tension, trying lowering the system free energy. This balance of free energy-reducing

attraction and electrostatic repulsion forces give rise to what is known as a Taylor cone or a Taylor instability at the tip of the discharging device[15]. Due to the pull of the electric field towards the grounded collection electrode and the unstable nature of the Taylor cone, a whipping instability develops, causing the liquid jet to be elongated and spun as it approaches the target. This effectively causes the solvent to evaporate and the formation of a solid polymeric fiber on the collection electrode. If needed, multiple polymeric streams can be combined into one via co-electrospinning, provided the polymeric solutions are mutually miscible. Modifications to this technology also exist, most notably the usage of a spinning collection drum or mandrill instead of a static collection plate, thus giving rise to aligned polymeric fibers[15].

The synthesis of an electrospun nanofibrous poly(D,L-lactide-co-glycolic acid) (PLGA) structure with randomly oriented fibers by Li *et al* in 2002 played a particularly pivotal role in the advancement of electrospinning as a viable synthesis tool[29]. Researchers in this publication cited the various properties such as pore size, cell-substrate interaction, and mechanical stiffness of the resulting PLGA mesh that would make for an ideal tissue scaffold. Indeed, studies performed by Li *et al* looking at cultures of human mesenchymal stem cells (hMSCs) on these PLGA scaffolds showed that cells growth was viable: the hMSCs appeared to adhere to the mesh and penetrate into the three-dimensional matrix, allowing for cell growth over seven days. Researchers postulated that the mesh's extracellular matrix (ECM)-mimicking geometry played a role in the proliferation of cells: a sentiment that has been echoed across a multitude of publications since then. The biodegradable properties of PLGA were also highlighted as a potential benefit due to its ability to naturally break down into non-cytotoxic and non-immunogenic components in an aqueous environment. Additionally, electrospinning presents several additional advantages over

other tissue scaffold synthesis techniques. For example, it does not allow for the presence of residual particulates in the matrix as sometimes can occur during particulate leaching, and allows for the usage of a very wide range of polymers in the synthesis process, a property that gas foaming cannot achieve due to the high levels of heat required.

Other fibrous mesh properties that have been of particular interest over the years includes fiber orientation, which can be defined as the average angle one fiber makes with another, with values ranging from zero to 90 degrees. A mesh with perfectly aligned fibers would thus have an average incident angle of zero degrees, while a perfectly, randomly unaligned mesh would have an average incident angle of 45 degrees. It should be noted that given a uniform fiber distribution, an unaligned mesh would may or may not have a higher pore size than an aligned mesh, due to the fact that inter-fiber spacing, which is primarily driven by solvent-polymer interactions during the spinning process, is not dependent on fiber alignment[15,16]. Previous publications have successfully demonstrated the effect that fiber orientation has cell proliferation, although the exact difference between aligned and unaligned fibers varies by cell type[30].

One particularly notable study in this direction was conducted by Liu *et al* in 2015, in which researchers looked at the effect of fiber orientation on the proliferation of rabbit annulus fibrosus-derived stem cells (AFSCs)[30]. In this study, freshly harvested AFSCs were seeded onto aligned and unaligned electrospun poly(ester carbonate urethane) -urea (PECUU) scaffolds, a more biodegradable formation of poly(urethane). In this study, researchers found that AFSCs seeded on aligned fibers tended to align themselves with the fibers and exhibited slightly elongated nuclei compared to their unaligned fiber counterparts, although cell proliferation did not differ significantly. The main difference occurred in molecular expression, particularly through the

production of type I collagen molecules: researchers found that in aligned fiber cultures, AFSCs produced almost twice the level of type I collagen compared to AFSCs grown on unaligned fibers, although type II collagen and aggrecan (a proteoglycan typically produced by AFSCs) expression levels were constant across both cultures. This study thus echoed the findings from various other studies that the geometry of an electrospun mesh may play a role in certain aspects of cell behavior, but not all. This phenomenon also has been seen to vary across different cell types, as reported in the literature.

AFM measurements of single fibers

The use of atomic force microscopy to determine the rigidity and topography of planar surfaces ranging from soft plastics to metals and ceramics has been a thoroughly studied topic[31]. Assuming that an AFM tip can be modeled as a single point force with magnitudes spanning 10^{-11} to 10^{-8} N, micron-diameter fibers will undergo beam deformation upon probing. Therefore, traditional AFM techniques are not ideal for studying rigidities on these types of substrates.

In order to more fully study the mechanical properties of single polymeric fibers, Baker *et al* utilized a novel fiber anchoring technique, which, coupled with an AFM tip, allowed researchers to more accurately calculate the Young's modulus, yield stress, relaxation time, and other properties[31]. In this study, which focused solely on PCL nanofibers fibers, researchers used a combination of lithography and electrospinning to form an array of single fibers that spanned rectangular troughs of controlled depth and width. By anchoring the ends of the fiber to the trough ridges as seen in figures 3A and B of their paper via a micropipette and UV-activated glue, researchers were able to use an AFM tip to apply a set tangential force to the PCL nanofiber. Then,

by measuring the deflection of the fiber in conjunction with the laterally applied force, researchers were able to construct an effective stress-strain curve. It should be noted that the glue was not observed to wick along the fiber and potentially skew rigidity measurements.

The mathematics used by Baker *et al* derive from fundamentals of solid mechanics. In reference to figure 3B of their paper, the force exerted on the PCL fiber can be determined via simple trigonometry. Using the displacement of the fiber and its original length, we can calculate the following, where F_{fiber} and $F_{lateral}$ are the forces experienced by the fiber and applied laterally by the AFM tip, respectively. That is, F_{fiber} were directed along the axis of the fiber whereas $F_{lateral}$ were perpendicular to the fiber's original conformation.

$$\beta = \tan^{-1}\left(\frac{s}{L_{initial}}\right) \qquad F_{fiber} = \frac{F_{lateral}}{2\sin\beta}$$

It should be noted that for this calculation, L_{inital} were one half of the un-stretched fiber length. Knowing F_{fiber}, we can proceed to calculate stress as usual with $\sigma = F_{fiber}/(\pi r^2)$. While r can be readily determined from microscopy data (i.e., SEM) assuming a cylindrical fiber, we need a way to calculate $F_{lateral}$.

There have been multiple equations suggested in the past to calculate $F_{lateral}$. The most fundamental approximation provided by Asay, Hsiao, and Kim[34] in 2006 of $F_{lateral} = F_{load}\cos\theta\sin\theta$ where θ represents one half of the complimentary angle to the angle of the applied force has merits in its simplicity, but has been shown to have inaccuracies as it does not take the mechanical properties of the tip into account. In order to circumvent this, Baker *et al* used the equation:

$$F_{lateral} = K_C I$$

In here, I is the strength of the left-right photodiode signal, which is measured in Amperes. K_C on the other hand, is the lateral force constant of the AFM tip, and is expressed in units of Newtons per Ampere:

$$K_C = S_n \left[\frac{Ewt^3}{6l^2(h + 0.5t)} \right]$$

In this equation, E represents the Young's modulus of silicon (taken as 1.690 x 10^{11} N/m^2), w, l, and t are the width, length, and thickness of the cantilever, respectively, and h represents the height of the cantilever tip. S_n denotes the normal force sensor response, which is measured in inverse amperes. With the exception of cantilever thickness, all of these variables were readily obtained from either microscopy or calibrations by Baker *et al*. In order to calculate cantilever thickness, researchers used the following equation, which relates cantilever properties to the resonant frequency f and the density of tip material ρ:

$$f = 0.276 \sqrt{\frac{Ewt^3}{\rho(\pi h^3 l^3 + 2.832 wtl^4)}}$$

Because the resonant frequency is known, one can reverse calculate t. Note that this equation only holds for silicon-based tips, but equations for other tip materials will follow the same form. Following this, researchers were able to calculate strain using the equation, where L' is one half of the length of the stretched fiber:

$$\varepsilon = \frac{L' - L_{initial}}{L_{initial}}$$

By plotting out the resulting stress-strain curves as seen in figure 5 of their paper, Baker *et al* were able to observe only a very small region of linear deformation followed by a much larger region of plastic deformation, with an overall graph whose slope was monotonically decreasing. These results indicated that their PCL fibers underwent significant strain-softening, as is common in polymeric materials. Specifically, the region of elastic deformation yielded an average slope of approximately 28 MPa over a range of strains from 0-3%. However, the average slope for the curve after the yield point (seen as approximately 30% in figure 5) was approximately 3.9 MPa.

This study primarily serves to highlight the differences between mechanical properties of the bulk material (i.e., Young's modulus) and measured mechanical properties of single fibers. Of particular note is the differences between measured fiber rigidities, which spanned single digit MPa, and the literature values Young's modulus of PCL, which can span from hundreds of MPa to single digit GPa. Similar experiments performed by other groups on PCL fibers with diameters in the 500 nm to 1 µm range have likewise resulted in a wide spread of measured rigidities, ranging from 100-500 MPa to as high as 1-3 GPa and 3-5 GPa for reasons that are not fully understood. Although different strain rates and molecular weights of PCL were used for these studies, ranging from 60-300 kDa, it is hypothesized that small deviations in strain rate or molecular weight alone are not enough to account for these wide discrepancies in measured tensile modulus.

In addition, Baker *et al* noted that there appeared to be a dependence of mechanical properties on the age of the fiber[31]. In comparing a freshly spun fiber to an aged fiber (defined as samples 30 days or older), researchers found that while new samples had an average strain limit of 19 ± 5%, aged samples had strain limits of only 8 ± 2%. This was further reflected in the measured rigidities of the samples, where new samples had total tensile moduli of approximately 62 ± 26 MPa, but

aged samples had total tensile moduli of 99 ± 84 MPa. The same phenomenon was observed for energy loss in a single fiber manipulation. Therefore, one can reasonably conclude from this experiment that for micro and nanoscale non-planar materials, measured mechanical properties may be different than the bulk material: processing may change mechanical properties.

It should be noted however that the PCL fibers used by Baker *et al* had diameters ranging from 440 nm to 1.04 µm. While the troughs (6.5 µm height, 13.5 µm span from ridge to ridge) represent length scales similar to what one would observe from a fibrous mesh of this material, the strain rate of the fibers was set at 300 nm/s, which may closely resemble what deformations a single cell attachment will cause to a single polymeric fiber.

Euler-Bernoulli theory

As previously discussed, the interaction between a single human T cell and an underlying mesh fiber will yield an estimated fiber deflection on the order of ten to one hundred nanometers. Because the deformations to mesh fibers are postulated to be small compared to the diameter of the micron-scale fibers themselves, Euler-Bernoulli beam theory presents itself as viable fundamental starting point for a model for mesh fiber, or beam, deflection[32]. Euler-Bernoulli beam theory, which first saw usage in mechanical engineering and design calculations for the construction of large structures such as Ferris wheels and the Eiffel Tower in the late 19th century, still sees usage today as a general, first-order estimate for the behavior of linearly elastic beams under various loading and support conditions, as well as beam cross-sectional geometries[33]. Regardless of load and / or support type, there are three fundamental assumptions to Euler-Bernoulli theory that apply themselves well to the current situation. Firstly, it is assumed that the

application of the load does not result in significant warping of the cross-sectional area of the beam itself. Although this is not entirely reflective of what occurs in reality, warping of the beam is postulated to be minute at best, and thus will not significantly impact the resulting mechanics. Secondly, the cross-sectional area of the beam remains planar and perpendicular to the loading axis. It should be noted that this final assumption is held, even in the case of beams with irregular geometries. Finally, it is assumed that rotational motion around the central axis of the beam is negligible, or in other words, that the cross sectional areas of the beam do not rotate upon application of the load[33].

At its most fundamental level, Euler-Bernoulli theory relates the deflection of a one-dimensional beam δ to the magnitude of the distributed, applied load q, where x represents the distance along the main axis of the beam, E is the Young's modulus of the bulk beam material, and I represents the moment of inertia. Note that both q and δ in the general case can be seen as functions of x due to non-uniform loading. Furthermore, since the flexural rigidity, herein defined as the product of E and I, is most often times constant, $q(x)$ can be directly related to the fourth derivative of the deflection function[32,33]:

$$q(x) = \frac{d}{dx^2}\left(EI\frac{d^2\delta(x)}{dx^2}\right) \approx EI\frac{d^4\delta(x)}{dx^4}$$

Calculation of the deflection for a given beam geometry and loading condition thus varies from case to case, but will generally require one to solve the fourth order differential equation above or a variant of it.

The case of a single cell residing on a beam, however, can be roughly approximated as a three-point bending scenario. In this situation, a beam with length L as described above sits on two simple supports at its ends and is subjected to a single asymmetric perpendicular point force at a position $x = a \in [0, L]$ along its length (see figure 3). The boundary conditions in this scenario indicate that $\delta(0, L) = 0$ and furthermore that $\frac{d\delta(a)}{dx} = 0$:

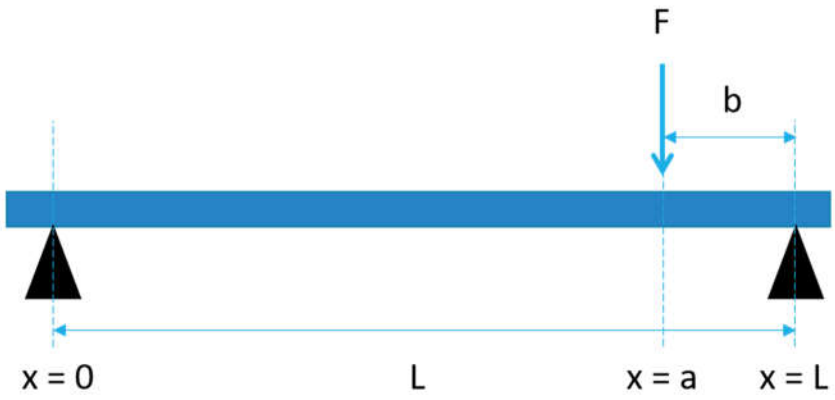

Figure 3: Asymmetric point loading of a beam with two simple supports

In this case, the solution to the differential equation yields the following equations for deflection $\delta(x)$ given a circular cross-sectional area[33]:

$$\delta(x) = \frac{Fx(L^2 - x^2)^{3/2}}{9\sqrt{3}LEI} \qquad I = \frac{\pi r^4}{4}$$

$$\delta_{max}(x) = \frac{\sqrt{3}Fb}{27}\left(\frac{(L^2 - b^2)^{3/2}}{LEI}\right)$$

Although a cell pushing down on a mesh fiber by itself is not a point force, we can approximate it as one due to the length scales of the cell and fiber involved in this situation. It should be noted

that in this scenario, additional assumptions, most notably that fiber slippage does not occur, were made on top of the fundamental assumptions characteristic of Euler-Bernoulli theory.

Additional modifications are commonly performed on the classic Euler-Bernoulli theory model to allow for more accurate prediction of a material's behavior[32,33]. One particularly common modification takes into account the shear modulus μ of the bulk material, thus giving rise to the material length scale parameter l. This parameter relates to the microscale size effect of the materials being probed: higher values of l (units in meters) are indicative of how far away from the load can the original Euler-Bernoulli approximations reflect up to 50% of the calculated deformation. The material length scale parameter therefore can be viewed as a cousin of the persistence length in polymer physics. In this case, $q(x)$ depends on both the flexural rigidity as well as the material length scale parameter. A in this context represents the cross sectional area of the beam in question:

$$q(x) = (EI + \mu A l^2)\frac{d^4\delta(x)}{dx^2}$$

With this in mind, the deflection $\delta(x)$ for an asymmetrically distributed non-point load becomes the following:

$$\delta(x) = \frac{Fx(L^2 - x^2)^{3/2}}{9\sqrt{3}L(EI + \mu A l^2)}$$

Research Question and Specific Aims

The main objective of this thesis is to explore the effect of electrospun microfiber fiber geometry on perceived cellular rigidity, and ultimately, reveal how this can affect human T cell mechanosensing. Understanding this phenomenon is of particular importance for potential leverage in clinical level T cell-based adoptive immuno-therapy and for fuller elucidation of T cell mechanobiology as a whole. In order to fully explore this topic, this thesis proposal is divided into two main specific aims, each with two respective sub-aims, as detailed below.

Specific aim 1: *Create a robust platform for the ex vivo expansion of human T cells*

This platform would ideally possess several characteristics to render it suitable for the *ex vivo* expansion of human T cells. Firstly, this substrate should be non-biodegradable in order to ensure that residual material does not leach into the cell media and subsequently, into the final cell transfusion into the patient. Secondly, to further ensure the lack of activating substrate in the cell infusion, this platform should be readily removable from the cell culture. A manifestation in the form of a single continuous sheet, as opposed to an array of disjoint microbeads, would satisfy this demand. Thirdly, the surface area to volume ratio of this platform should be maximized in order to yield a similar level of functional area as compared to the clinical gold standard. Fourthly, this platform should be synthesized in a manner that is readily scaled to high throughput levels in order to facilitate its development and eventual deployment on a clinical scale. Finally, however, the main goal of this platform is to create high numbers of functional human T cells. Evaluation criteria towards this end will thus be based not solely on cell number, but also on cell activation and cell phenotype. The ramifications of this part of the thesis include the further development and

commercial realization of ACT. We hypothesize that this can be effectively done through the synthesis of a microfibrous PDMS-based mesh in order to simultaneously leverage T cell mechanosensing while satisfying the aforementioned design criteria. To better study this segment of the project, we will divide this aim into two sub aims below: one focusing on the design of the platform itself, and one focusing on the cells produced from this platform.

Specific aim 1a: *Design, fabricate, and characterize a 3D fibrous PDMS/PCL mesh for T cell stimulation*

This thesis effectively builds off of the work previously performed by O'Connor *et al* and Judokusumo *et al* by investigating how human T cells respond to surfaces of varying rigidities in the 10^5-10^6 Pa range, but while also maintaining the high surface area to volume ratio characteristic of submicron-based activating bead platforms. Although an array of soft microbeads would achieve both goals, our goal is to improve upon the safety of magnetic microbead-based platforms by developing a platform that would be removable from the cell solution in one step. This would be readily accomplished through the development of a 3D electrospun microfibrous mesh. As a well-studied, high-throughput technique, electrospinning presents itself as a facile method for synthesizing our proposed meshes. Although a wide range of natural and synthetic polymers have been previously used in electrospinning, spanning from collagen and alginate to poly(vinyl chloride) and poly(urethane), the primary mesh material in this matter was chosen to be PDMS due to its rigidity modulatory properties through modification of the crosslinker to base ratio, as well as its non-cytotoxicity and non-biodegradability. However, as previous literature has suggested, the electrospinning of pure PDMS microfibers has yet to be accomplished, in part due to the highly viscous nature and organic solvent immiscibility of this polymer. To aid in the

electrospinning process, we herein blend PDMS with PCL, an economical, non-cytotoxic, non-immunogenic, commercially available polymer. Although the addition of PCL to the mesh will undoubtedly raise the rigidity, its role as a viscosity modulator is be vital to mesh synthesis. Optimization of mesh spinning parameters, such as working distance, voltage, polymer feed concentration, and spinning rate, were necessary to tune mesh fiber geometry. In order to optimize cell interaction with the mesh, it was postulated that fibers with diameters greater than 10 μm and pore sizes with diameters less than that of a resting T cell, taken as 7 μm, would not be optimal in promoting expansion. Previous studies on proliferation with cell types ranging from AFSCs[30] to human fibroblasts[29] have tested the effect of fiber alignment on cell growth. To test the effect of fiber alignment on cell activation and proliferation, both unaligned and aligned meshes were synthesized by the use of a stationary collection electrode or rotating drum, respectively.

It should be noted that PDMS has a network polymer structure and is thus has a particularly high permeability to a range of small hydrophobic molecules, most significantly, gases such as oxygen[13]. As such, some applications see the use of PDMS as a modulator to determine how much gas enters a particular chamber or partition. On the other hand, the use of PDMS in applications such as microfluidics and more macroscale implants is generally avoided due in part to its ability to reduce oxygen concentrations in cell cultures. In this application, cells are cultured on PDMS-based scaffolds, however, due to the small amount of PDMS present, the effects of oxygen and other small molecule absorbance are hypothesized to be negligible.

In order to maximize the surface area to volume ratio, while still maintaining adequate room for cell penetration into the mesh, we have synthesized both microscale and nanoscale diameter

fibers through the modulation of the aforementioned spinning parameters, most prominently, polymer concentration in the spinning feed. Pore size was also of importance, as pores with diameters on the same order as of a naïve T cell would be conducive towards cell penetration into the mesh, thus taking full advantage of the high surface area to volume ratio. Verification of mesh morphology was performed via SEM, however, to ensure even dispersion of PDMS and PCL molecules in the final fiber, Fourier transform infrared spectroscopy (FTIR) was also performed. Bulk rigidity values were calculated via uniaxial tensile testing and AFM measurements on casted, planar samples, while local fiber rigidities were measured solely by AFM. The overall goal of this section is thus to synthesize PDMS/PCL meshes with tunable microscale and nanoscale fiber diameters and pores, and we hypothesize that electrospinning will present itself as an excellent choice of synthesis process.

Specific aim 1b: *Evaluate the effects of rigidity modulation in electrospun PDMS/PCL meshes on human T cell activation and proliferation*

This section of the thesis aims to analyze how fibrous mesh properties, such as rigidity, fiber alignment, and pore/fiber diameter affect human T cell activation and proliferation. We hypothesize that better leverage of T cell mechanosensing, as realized in the formation of softer experimental meshes, will yield higher levels of cell proliferation while maintaining or improving cellular activity and maintaining cell phenotypic distributions. In order to provide T cells with the activation signals required for stimulation, meshes were coated with agonist antibodies to surface proteins CD3 and CD28: these provide the primary and secondary activation signals for T cells, respectively. A primary/secondary antibody capture technique were used to adhere the activating

antibodies to the surface of the mesh and ensure that activating antibodies will have the proper, upward-facing orientation.

Isolated human T cells from whole blood from healthy donors aged 18 to 64 were then stimulated on these meshes. In order to prevent overstimulation and thus premature cell death, T cells were removed from the mesh environment after three days and allowed to continue growing in a mesh-free environment. During this time, cell proliferation, size, and activation were monitored. Two key measurements of this were the proliferative index (PI), which measures the average number of divisions a cell has gone through, and the percent of cells entering primary division (% div).

Upon completion of the primary blasting phase, cells were further assayed for activation and phenotype markers in order to determine the distribution of effector memory, central memory, effector, and naïve cells in culture, we were assaying for surface markers CCR7, CD45RO, and CD62L, in addition to the standard markers for helper T cells and cytotoxic T lymphocytes (CTLs), CD4 and CD8, respectively. To analyze the activation level of $CD4^+$ cells, we were assaying for IFNγ, a cytokine secreted by helper T cells. Likewise, we were assaying for the expression of lysosomal-associated membrane protein-2 (LAMP-2), or CD107b, in order to measure the activation level of cultured $CD8^+$ cells. Finally, to further mimic the current model of adoptive immunotherapy, a subset of the total cell culture was isolated and frozen down prior to being restimulated and analyzed for all surface markers and cytokines.

In addition, it has been previously noted that the Dynabead® platform has had difficulty with inducing the activation and proliferation of exhausted T cell populations, such as in patients suffering from chronic lymphocytic leukemia (CLL). In order to measure the effectiveness of our

mesh platform on the expansion of exhausted T cell populations, we conducted the T cell activation and proliferation experiment in this section with cells isolated from CLL patients of Rai stages 0-4 in addition to cells from healthy patients as controls.

Specific aim 2: *Develop and validate a quantitative model for mesh rigidities on a cellular scale*

Although it has been successfully demonstrated that human T cells undergo mechanosensing, as previously discussed, cells residing on a fibrous mesh may not perceive the underlying rigidity in the same manner as it would a bulk, planar surface. One analogy in this case would be that of a person climbing a rope ladder: although the rope is hard and rigid to the touch, a person ascending said ladder will most likely perceive it supple and yielding to the mechanical forces associated with climbing. A single cell residing on a mesh fiber will thus experience both the local Young's modulus of the fiber material itself as well as the soft, macroscopic bending motion of the beam. By establishing a model that more accurately describes what T cells experience on a mesh, we can better correlate results from this experiment with existing reports in the literature on T cell stimulation on planar surfaces. On a broader scale, this section of the thesis aims to widen the understanding of T cell mechanosensing and mechanobiology as a whole. It should be noted however that this section of the thesis does not focus on elucidation of the precise biology of T cell mechanosensing: while it will yield insight into what forces the cell experiences on the mesh, questions such as which proteins are involved in the mechanosensing process, what the signaling pathway is, and what traction forces are exerted by the cell on the mesh will not be addressed. These questions, while important for the complete understanding of T cell mechanobiology, are not yet fully studied and will be addressed in future studies performed by this lab.

Specific aim 2a: *Develop a quantitative model for mesh rigidities on a cellular scale*

The goal in this part is to explore how microscale fiber geometries impact measured rigidities and thus give insight into what a T cell feels when interacting with the mesh. Although AFM imaging can provide excellent topographical and surface geometry data, its insight into the exact rigidity of the material is somewhat attenuated by the fact that beam deflection and material deformation were non-negligible factors for a microfibrous mesh. This part of the study therefore builds off of the study performed by Baker *et al*, in part.

To explore this phenomenon, AFM measurements on single fibers were performed with varying peak force set point levels (pFS) from 10^{-8} to 10^{-10} N and peak force amplitude (pFA) levels from 10 to 200 nm. As our synthesized meshes will have rigidities in the 10^{5}-10^{6} Pa range, we were using tips with relatively low cantilever spring constants ($k < 1$ N/m). Tip diameters were kept to a minimum ($d < 40$ nm) in order to obtain the sharpest images possible of mesh topography and rigidity mapping. Furthermore, we will explore how and if measured mechanical properties of fibers change over time by testing freshly prepared meshes alongside meshes aged three months or more. By combining the AFM data from material deformation, tip adhesion, tip indentation, and mechanics of beam bending via Euler-Bernoulli theory, we calculate out a more accurate measurement of what the cell is seeing on the mesh, and summarize this into a unifying model.

Specific aim 2b: *Assess the validity of the mesh rigidity model via an in vitro cell-based study*

In the final section of this thesis, we aim to validate the accuracy of our model derived in specific aim 2a in reflecting the perceived rigidity of PDMS/PCL meshes. To this end, a follow-up *in vitro* study was performed. In this part of the experiment, electrospinning parameters were re-tuned in

order to synthesize meshes with perceived rigidities on par with the planar surfaces analyzed in O'Connor *et al*'s study, most notably polymer weight concentration, working distance, and solution discharge rate. Specifically, mesh fibers were fabricated to yield perceived rigidities, or effective Young's moduli, equal to approximately 1 MPa and 40 kPa. Human T cells isolated from healthy donors were once again be cultured upon these substrates as outlined in specific aim 1b, and additional experiments for IL-2 secretion were performed to compare with the results from O'Connor *et al*'s study. By validating this model, this experiment effectively establishes a baseline for rigidity measurements of microfibrous meshes in which beam bending motion plays an important role in the calculation of effective Young's modulus.

Methodology

Specific aim 1a: *PDMS/PCL mesh fabrication and characterization*

1.1 Mesh fabrication and functionalization

Fibrous meshes were synthesized via co-electrospinning of NuSil MED-4086 PDMS (M4086) or Sylgard 184 PDMS (S184) mixed with PCL (Sigma, M_n = 80 kDa) in a 3:1 v/v solution of dichloromethane (DCM) / N,N-dimethyl-formamide (DMF) at 8-10 kV onto either a grounded static collection electrode or rotating drum with a working distance between 8-12 cm. For M4086 fibers, either a 1:1 or 5:2 w/w ratio of PDMS:PCL (herein termed low [PDMS] and high [PDMS] respectively) were used, while for S184 fibers, a 1:1 or 4:1 ratio of PDMS:PCL were used. Mesh spinning times were varied between 5 and 8 hours, and all meshes were allowed to sit overnight at room temperature prior to use. Additionally, meshes of pure PCL were electrospun as rigid controls.

Meshes were coated with goat-anti-mouse IgG linkers (MP Biomedicals, 2 µg/mL, Cat no. 0867028) at room temperature for 2 h followed by a 1:4 mol/mol ratio of mouse IgG-anti-human CD3 (Bio X Cell, clone OKT3, Cat no. BE0001-2) to mouse IgG-anti-human CD28 (Bio X Cell, clone 9.3, Cat no. BE0248) at room temperature for 2 h (2 µg/mL total solution). Blocking were performed with 5% bovine serum albumin (BSA) (Sigma, lyophilized powder, $\geq$ 96% via agarose gel electrophoresis, Cat no. A9418) at room temperature for 2 h. For cell expansions, meshes were secured to glass coverslips via a thin layer of partially cured S184 PDMS (1:3 w/w crosslinker to base ratio) (see fig. 2). Prior to cell seeding, meshes were sterilized with an ethanol bath at room temperature (70%, 30 min) followed by UV irradiation for an additional 30 min and drying in air for a final 30 min.

1.2 Mechanical and chemical analysis of meshes

Mesh fiber and pore sizes were quantified via scanning electron microscopy (SEM) (Hitachi S-4700, 1.5 kV). Samples were coated with a thin layer of Au-Pd via sputter coating in Argon (Cressington 108, 12-15 s) prior to SEM analysis. Bulk and local rigidities were quantified via a uniaxial tensile tester (Instron 8841) and via atomic force microscopy (AFM) (Bruker Multimode 8 with QNM), respectively. Mesh chemistries were analyzed via Fourier transform infrared spectroscopy (FTIR-ATR) (DigiLab Excalibur).

Specific aim 1b: *Human T cell expansions on synthesized PDMS/PCL meshes*

1.3 Patient samples

Mixed naïve $CD4^+$ / $CD8^+$ T cells were isolated from whole blood derived from healthy patients aged 18-64 years or CLL patients currently at Rai stages 0-4 inclusive. Briefly, cells were incubated with RosetteSep for 25 min (5% v/v) (Stemcell Technologies, Cat no. 15061) prior to centrifuging (Eppendorf 5810R, 25 min, 800 x G) in Ficoll-Paque PLUS (GE Healthcare, Cat no. 17-1440-02). Cells were frozen in 10% v/v DMSO and kept in liquid nitrogen for up to two years.

1.4 T cell activation and proliferation

Prior to seeding, isolated T cells were treated with carboxyfluorescein succinimidyl ester (CSFE) (Thermo-Fisher Scientific, Cat no. C34554) in order to track cell division and proliferation. T cells were seeded onto meshes or with Dynabead® positive controls (Thermo Fisher, Human T Cell Activator, Cat no. 11132D) according to the manufacturer's recommendation in a 24-well plate (Corning, Cat no. 3524) at a density of 1 million cells / mL and cultured for 3 days (37°C, 5% CO_2).

Cells were removed from meshes via manual pipetting or a magnetic wand for Dynabeads®. Cultures were counted and reseeded at 1 million cells / mL on day 3 and every other subsequent day without activating substrates in a 12-well plate (Corning, Cat no. 3513) for a total of up to 19 days.

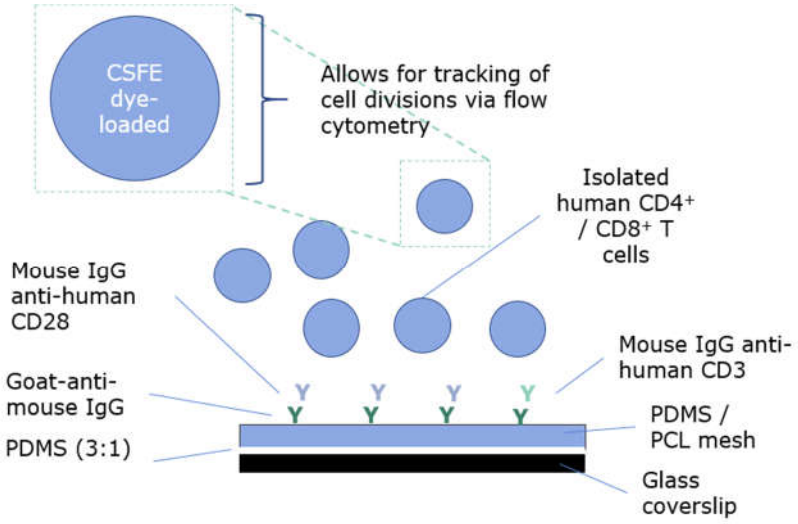

Figure 4: Mesh configuration schematic for cell expansions

RPMI 1640 media (Gibco, Cat no. 21870-076) supplemented with L-glutamine (20 µM, Gibco, Cat no. 25030-081), fetal bovine serum (FBS) (5%, GE Healthcare, Cat no. SH30071), 1x penicillin streptomycin (Thermo-Fisher Scientific, Cat no. 15140122), and HEPES (100 µM, Sigma, Cat no. 3784) were used for all culture steps of this experiment.

Flow cytometry (BD FACSCANTO II, BD LSRFortessa) were performed on days 3 and 5 of culture to track cell proliferation and activation. Additionally, cell phenotype was determined by staining for surface proteins CD4, CD8, CD45RO, and CCR7. Cell size were tracked via a handheld particle counter (Millipore Scepter® 2.0) beginning on day 3 and every other subsequent day until mean cell volume dropped below 400 fL.

1.5 T cell restimulation and cellular activation assays

T cells were frozen upon completion of the initial blasting phase post-primary stimulation, herein defined as when average cell volume dropped below 400 fL. For restimulation, cells were thawed, allowed to rest for 12-14 hours, and subsequently stimulated on Dynabeads® according to manufacturer's recommendations.

Cell activation were quantified through expression of CD107b (lysosome-associated membrane protein 2, LAMP-2) and interferon gamma (IFNγ). For CD107b, cells were thawed and restimulated for 4 h on Dynabeads® while for IFNγ, cells were allowed 12 h for restimulation on Dynabeads®. Staining were performed according to manufacturer's recommendation (Biolegend, Clone H4B4, Cat no. 354304; Miltenyi Biotec, Cat no. 130-090-433, respectively). Additionally, staining for perforin (Biolegend, Clone dG9, Cat no. 308118) were also performed in accordance with manufacturer's protocol.

1.6 Cell exhaustion assays

CLL patient-derived cells were stained for programmed cell death protein 1 (PD-1, CD279) (Biolegend, Clone 1A12, Cat no. 135214) on day 0, day 3, and every other subsequent day until mean cell volume dropped below 400 fL.

1.7 Protein desorption assays

In order to measure protein desorption, cell-free meshes were coated with goat-anti-mouse IgG linkers at room temperature for 2 h followed by a 1:5 mol/mol ratio of FITC-tagged mouse IgG-anti-human CD3 (Biolegend, clone OKT3, Cat no. 317306) to non-fluorescent mouse IgG-anti-

human CD3 (Bio X Cell, clone OKT3, Cat no. BE0001-2) for 2 h. Meshes were incubated in RPMI media for 2 days at 37 °C and were subjected to epifluorescence imaging at either day 0, 1, or 2 (Olympus IX71). Microscopes were calibrated via fluorescently labeled microbeads prior to imaging (Inspek Green 505/515).

1.8 Cell inhibition assays

Cell inhibition assays were performed via addition of ROCK inhibitor Y-27632 (compound Y, Stemcell Technologies) to cell cultures at 5, 1, 0.5, 0.1, and 0 µM. Prior to seeding and after FITC treatment, cells were incubated in compound Y for 20 minutes. Subsequent cell culture days were carried out with the same inhibitor concentrations as on day 0, and cell proliferation recorded in the same manner.

Specific aim 2a: *Quantitative model for PDMS/PCL mesh rigidities*

2.1 Rigidity measurements

Mesh surface topographies and rigidities were measured via atomic force microscopy (AFM) with a sharp conical tip (Bruker Multimode 8, SCANASYST-air tip, k = 0.4 N/m, d = 8-30 nm, cone half angle = 12-22°). Additionally, material deformation, tip adhesion, and tip deflection were measured. Lateral probe motion was limited to 1.0 µm/s. All AFM images were analyzed via AFM data processing software (Nanoscope 1.9) and subsequent curve fitting analyses were performed via Matlab (R2017a).

Standard Euler-Bernoulli theory for a simply supported beam with circular cross-sectional area subjected to an asymmetric point force was used as the starting point for model construction.

Specific aim 2b*: In vitro study for quantitative model verification*

2.2 Mesh fabrication and in vitro verification study

In order to verify the model developed in specific aim 2a, fibrous meshes were again synthesized as previously described, but with rigidities of approximately 150-300 kPa and 2-3 MPa in order to align with the tested bulk moduli of the paper by O'Connor *et al*. Electrospinning parameters were held constant as in specific aim 1a, but polymer concentrations were varied from 10 to 50% total weight percentage, working distance varied between 4 and 10 cm, and spinning speeds varied between 0.5 and 1.6 mL/h with a 25 G needle. Mesh spinning times were held constant at 5-8 hours and meshes were allowed to sit overnight at room temperature prior to use. *In vitro* studies of cell proliferation and activation were performed as previously described in methodology sections 1.4-1.6.

Results and Discussion: Specific Aim 1

Specific aim 1a: *PDMS/PCL mesh fabrication, functionalization, and characterization*

The main goal of this work is the engineering of a continuous platform that not only leverages mechanosensing but also retains the high surface area to volume ratio characteristic of microbeads. Centra7l to this is the ability to effectively tune the mesh fiber diameter and pore size to allow for cell penetration into the mesh matrix while maintaining a relatively soft overall material. As such, two key parameters that were varied alongside mesh rigidity were fiber diameter and fiber alignment in order to produce both micro and nanoscale mesh fibers in both aligned and unaligned forms. Modulation of various electrospinning parameters such as working distance, polymer weight concentration, and accelerating voltage allowed for the formation of a wide range of fiber geometries.

The grade of PDMS utilized in the formation of the meshes presents itself as another point of discussion, primarily due to the fact that only certain formulations are permitted by the FDA for use in the body. Typical manifestations of PDMS in the human body come in the form of cosmetic and reconstructive implants, i.e., breast implants. While the *ex vivo* nature of the expansion process for ACT does not readily lead to dissociation of activating substrate into the cell transfusion, using a grade of PDMS pre-approved for use in the body will better ensure that in the occasion should such a dissociation occur, the potential for patient harm will be negligible. Preliminary experiments in mesh synthesis and cell expansion utilized the S184 formulation due to its commercial availability and more widespread usage, particularly as an insulating material from electrical currents in transformers and printed circuit boards. However, S184 is not approved for

use in the human body, therefore the vast majority of results discussed herein will be focused on meshes synthesized with MED formulation due to the widespread usage of MED formulations (MED-6400, MED-2174, etc.) in implants and other products designed for long-term placement in the body. Furthermore, PDMS/PCL meshes made with a 1:1 w/w ratio of PDMS to PCL will herein be referred to as low [PDMS] meshes while meshes made with a 5:2 w/w ratio of PDMS to PCL will be referred to as high [PDMS] meshes. Note that the prefixes low and high refer only to their PDMS concentration, not the rigidity of the surface.

Electrospun aligned and unaligned M4086 fibers were found to exhibit a range of fiber diameters and pore radii ranging from 680 ± 290 nm to 2.28 ± 0.39 µm, and 2.51 ± 0.80 µm to 12.21 ± 3.37 µm, respectively via SEM (see figure 5). Unaligned fibers revealed an average angle θ between any two fibers was 35.15 $\pm$ 4.17°, while aligned fibers revealed $\theta \approx -5.22 \pm 3.29°$, thus indicating that fibers were indeed unaligned or aligned, respectively. Although well-defined fibers were observed to appear on the collection electrode, premature processing and utilization of these meshes indicated that fibers were not fully dry upon completion of spinning. As the electrospinning of pure PCL fibers do not normally give rise to this phenomenon, this wetness may indicate that submicron level PDMS units do not undergo crosslinking with solvent evaporation, but with lower levels of heat and time as well. In this experiment, nanoscale and aligned formulations were found to yield meshes with lower fiber diameters and pore sizes than their microscale and unaligned counterparts, respectively. Notably, significant differences in pore size, fiber diameter, and overall fiber morphology were not detected between S184 and M4086 PDMS meshes: on average, fiber diameter and pore sizes differed by less than 14%, with no formulation being consistently higher or lower in measurement than the other.

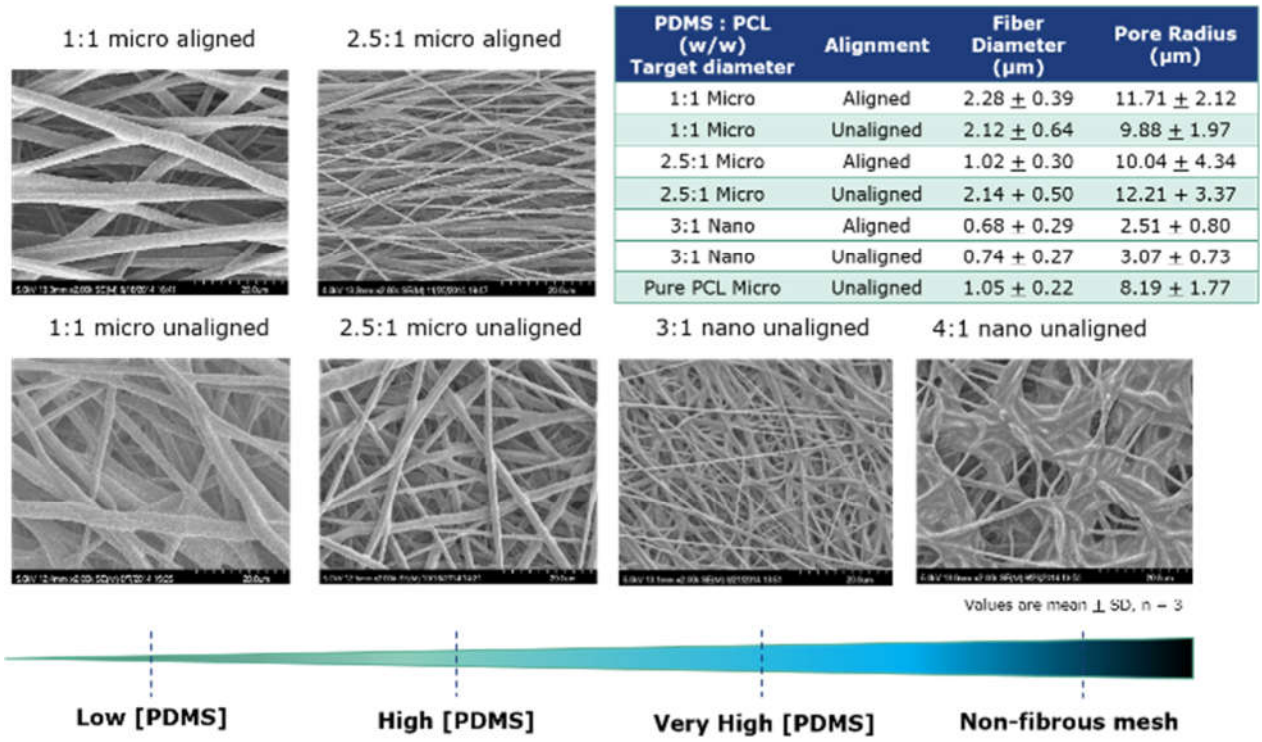

PDMS : PCL (w/w) Target diameter	Alignment	Fiber Diameter (µm)	Pore Radius (µm)
1:1 Micro	Aligned	2.28 ± 0.39	11.71 ± 2.12
1:1 Micro	Unaligned	2.12 ± 0.64	9.88 ± 1.97
2.5:1 Micro	Aligned	1.02 ± 0.30	10.04 ± 4.34
2.5:1 Micro	Unaligned	2.14 + 0.50	12.21 + 3.37
3:1 Nano	Aligned	0.68 + 0.29	2.51 + 0.80
3:1 Nano	Unaligned	0.74 + 0.27	3.07 + 0.73
Pure PCL Micro	Unaligned	1.05 ± 0.22	8.19 ± 1.77

Figure 5: SEM images of aligned (top) and aligned (bottom) M4086 meshes at varying ratios of PDMS:PCL (w/w), along with average fiber diameters and pore radii (n = 4). All images are taken at 500 X magnification. Higher concentrations of PDMS were observed to lead to non-fibrous mesh formation, as seen in the 4:1 nano formulation.

Microscale M4086 meshes were found to have fiber diameters on the order of 1-3 µm and pore sizes on the range of approximately 9-12 µm. Pure PCL meshes exhibited pore sizes and fiber diameters similar to those of other PDMS/PCL meshes. While high [PDMS] meshes tended to have larger fiber diameters and pore sizes than their low [PDMS] counterparts, this difference was less than 20% and thus was not considered to be significant factor in this experiment.

Ideally, we are looking for the mesh with the lowest possible PCL concentration, as its stiffness adds undesired rigidity into the mesh mechanical properties: mixing just a hair of PCL would thus

be ideal, as it ensure that one retains the viscosity-modulatory properties while minimizing rigidity. However, as seen from our experiment, (see figure 5), attempts to make 3:1 or 4:1 w/w PDMS/PCL meshes did not yield promising results. At the 3:1 ratio, fibers were seen to start to blend together. This became more prevalent at the 4:1 ratio where in lieu of steady electrospinning, the polymer feed would fly in macroscopic, intermittent blobs towards the collection electrode. This effectively let to the formation of a polymer mat with low pore sizes and irregular structure (see figure 5), rather than a mesh. Without sufficient levels of viscosity modulator present in the polymer feed to counterbalance the high levels of PDMS, the feed became unsuitable for electrospinning.

As the average diameter of a naïve human T cell is approximately 7 µm[12], it was hypothesized that pore sizes on the order of 9-12 µm would be optimal for cells to burrow into the mesh as opposed to nanoscale and aligned meshes, which featured pore sizes of approximately 2-5 µm. This would allow cells to fully take advantage of the high surface area to volume ratio characteristic of fibrous meshes. To confirm this, epifluorescence microscopy was conducted on meshes coated with a 1:5 mol/mol phycoerythrin (PE)-stained OKT3 / non-fluorescently tagged OKT3 at six hours post-seeding with isolated human T cells with a FITC-phalloidin stain for actin (see figure 6A). The resulting images confirmed that cells were interacting with the mesh and penetrating into the mesh matrix at depths up to 30 µm. As synthesized meshes were measured to have thicknesses of up to 120 µm, this indicated that there may be other forces preventing the complete penetration of cells into the mesh, such as the seeping of the PDMS glue layer up into the mesh during the mounting process, and / or the lack of penetration of activating antibodies into the mesh matrix. PDMS and PCL are notably hydrophobic molecules and while antibody adsorption

onto these surfaces will be an energetically favorable interaction, their dispersal in cell media, an aqueous medium, may not fully promote this adsorption.

It should be noted that while PCL is fully miscible in DCM and DMF, PDMS is not fully miscible in either. According to previous reports published by Lee *et al* in 2003[35], PDMS is most miscible in secondary and tertiary amines such as diisopropylamine and triethylamine, as well as slightly polar organic solvents such as diethyl ether. On the other hand, it is least soluble in alcohols (i.e., propanol, glycerol, etc.), di-substituted amines such as DMF, and water; essentially, organic solvents with moderate to high dipole moments (defined as $\mu > 1.4\,D$). Therefore, it is not feasible as of this writing to simultaneously force both PDMS and PCL into a perfect solution in DCM and DMF. An emulsion, formed by the incomplete but uniform dispersal of PDMS in a PCL-DCM/DMF solution was thus used as the electrospinning feed. To boot, emulsions were observed to phase separate if left static on a flat surface overnight, although emulsions were not observed to separate over the course of a single electrospinning session, i.e., 5-6 hours. Therefore, one key insight was to determine the level of dispersal of PCL in PDMS.

Chemical analysis of fibers via FTIR and correlation with the literature on the PDMS spectrum confirmed the presence of both PCL and PDMS peaks in the mesh (see figure 6B). This notion was later supported by AFM data, which will be fully discussed in a later section. AFM data revealed a relatively uniform local rigidity across the body of mesh fibers free of pockets of abnormally high or low rigidity, thus indicating that phase separation of PCL and PDMS was negligible during the electrospinning and drying process. As both S184 and M4086 meshes yielded very similar results in terms of physical properties and ease of electrospinning, the remainder of this report will primarily focus on M4086-type meshes due to its approval for use in the human body.

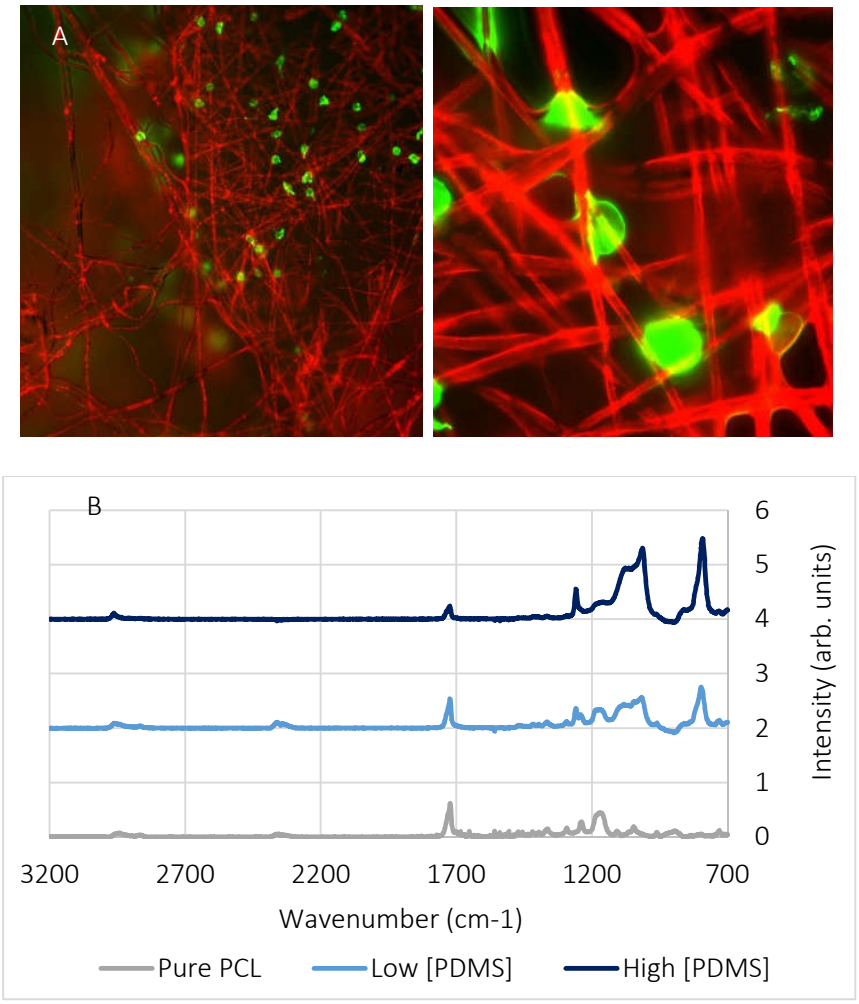

Figure 6: (A) T cell (green, FITC-actin) penetration and interaction with M4086 unaligned microscale low [PDMS] mesh fibers (red, PE-OKT3) at 20 X and 100 X magnification six hours post-seeding (left and right, respectively). (B) FTIR analysis for PDMS/PCL and pure PCL meshes. Note the presence of the characteristic PCL peak at 1728 cm^{-1} in all samples but lack of PDMS peaks in the pure PCL sample.

Functionalization of the mesh with primary capture antibodies and secondary activation antibodies via direct adsorption as previously performed by O'Connor *et al*. allowed for the proper orientation of activating antibodies for cell stimulation. However, as cells are stimulated on the

mesh for three days, a lack of protein desorption from the mesh into the cell media is of particular importance in order to prevent overstimulation and to ensure a safer transfusion to the patient. In this part of the experiment, meshes were coated with goat-anti-mouse IgG linkers at room temperature for 2 hours followed by another 2 hours with a 1:5 mol/mol ratio of FITC-tagged to non-fluorescently tagged OKT3 to approximate the primary / secondary antibody stack used on the meshes for expansion.

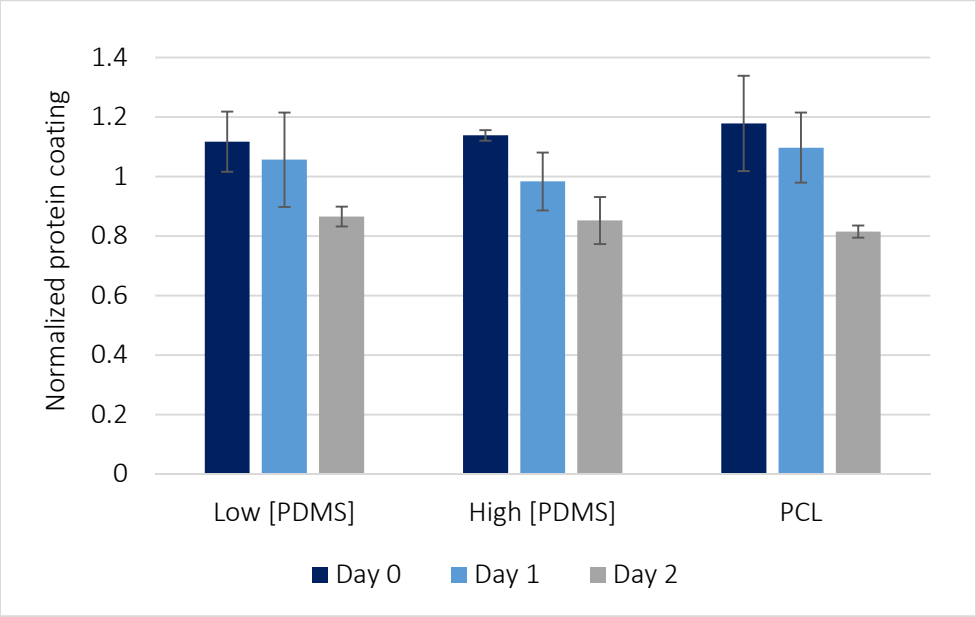

Figure 7: Protein coating concentration and desorption on days 0-2 inclusive (n = 3), normalized to the average protein concentration. All error bars mean ± standard dev.

Measurement of protein desorption across three days revealed a minimum of 80% antibody retention, thus suggesting minimal protein loss during the activation period (see fig. 7). Furthermore, protein desorption profiles were not found to differ significantly between mesh types, thus indicating that it is not protein adsorption concentration that is driving any differences in cell proliferation and activation levels, but more the underlying material itself. It should be noted

that although this was achieved without the usage of a covalent linking molecule scheme (i.e., biotin and streptavidin), future work, as discussed in the final sections of this thesis, will focus on development of such a linking strategy to ensure a safer patient transfusion.

Specific aim 1b: *Evaluate the functionality of PDMS/PCL meshes via T cell expansions*

Central to the clinical adoption of a platform for T cell based ACT is the ability to produce optimal amounts of active, viable T cells. According to recent papers, the benchmark of approximately 50 million cells per infusion has been postulated as the minimal amount. It should be noted that in healthy individuals, naïve T cells occur at a rate of approximately 1 million cells per mL of unprocessed whole blood. In patients suffering from certain maladies, such as early-stage leukemia, this number often times decreases due to the overproduction of other types of cells. In this case, early stage leukemia patients' immune systems are flooding the blood with large amounts of inactive, defective B cells, thus lowering the T cell concentration per unit volume[13]. Furthermore, the withdrawal of large amounts of blood from elderly patients and patients suffering from acute illnesses may often be undesired. Since excess cultured cells can always be frozen down and stored for future transfusions, it is in the best interest of the patient and the clinic to be able to produce as many cells as possible from a starting population while maintaining high levels of cell activation.

In order to have a viable cell transfusion however, cells must be both active and have the proper phenotypic distribution. Cell activity for non-regulatory T cells can be broadly concerns the production of cytokines such as IL-2, IFNγ, TGF-β, etc. by $CD4^+$ cells and the expression of cytotoxic surface markers such as CD107a (LAMP-1) and CD107b (LAMP-2) by $CD8^+$ cells. While the

production of regulator T cells via ACT may prove useful in the treatment of autoimmune diseases, the development of such therapies are outside of the scope of this project and thus, we did not aim to produce high levels of T_{reg}s from isolated naïve T cells. As previously stated in this report, the production of both effector memory and central memory T cells, as opposed to non-memory type T cells, were of particular interest to us since secondary stimulation of the adaptive immune system is mostly driven by memory cell subtypes rather than shorter-lived effector cells.

Long term cell culture for 19 days revealed similar growth patterns in both mesh and Dynabead®-expanded cells, with a primary blasting phase lasting anywhere between 7 and 11 days before returning to rest, as measured by cell volume (see fig. 8A). During this primary blasting phase, cells from all mesh and bead cultures were seen to undergo rapid division, as evidenced through the formation of cell clusters in solution. In order to gain an accurate perspective on cell volume, all particles with volume less than 200 fL (that is, the volume of a naïve T cell) were gated out as cell debris. Notably, cell debris was commonly observed in all mesh and bead cultures during the blasting phase. Cell volume typically peaked at day 5 at approximately 700 – 900 fL, although there was a small variation between cultures: some cultures would experience peak cell volume at day 7 instead of day 5, but during the course of this project, it was never observed that this peak happened anywhere before day 5 or after day 9. In contrast to mesh and bead cultures, negative control cultures, which comprised of isolated naïve T cells being seeded onto a planar polystyrene cell plate without the addition of cytokines or antibodies, did not experience growth throughout this period: cell populations typically reached near-zero figures after seven to nine days. This was expected, as without stimulation of the TCR, T cells are programmed to undergo apoptosis.

A key observation in this experiment was that improved cell expansion on PDMS/PCL meshes over pure PCL meshes and Dynabead® controls was achieved (see fig. 8B). Specifically, low [PDMS] and high [PDMS] meshes yielded approximately 9.4 ± 0.6 and 9.8 ± 0.6 maximum doublings, respectively, compared to 6.1 ± 0.9 and 7.3 ± 1.1 maximum doublings for pure PCL and Dynabeads®, respectively, thus implying that the mesh platform has the potential to produce upwards of 5.6-12.5 times more cells than the clinical gold standard. Although cell proliferation levels for both low and high [PDMS] meshes were significantly different from PCL meshes and Dynabeads® ($p < 0.05$, one-way ANOVA), there was not a significant difference between the low and high [PDMS] meshes themselves. This may likely be due to a relative similarity in rigidity levels (1:1 w/w compared to 2.5:1).

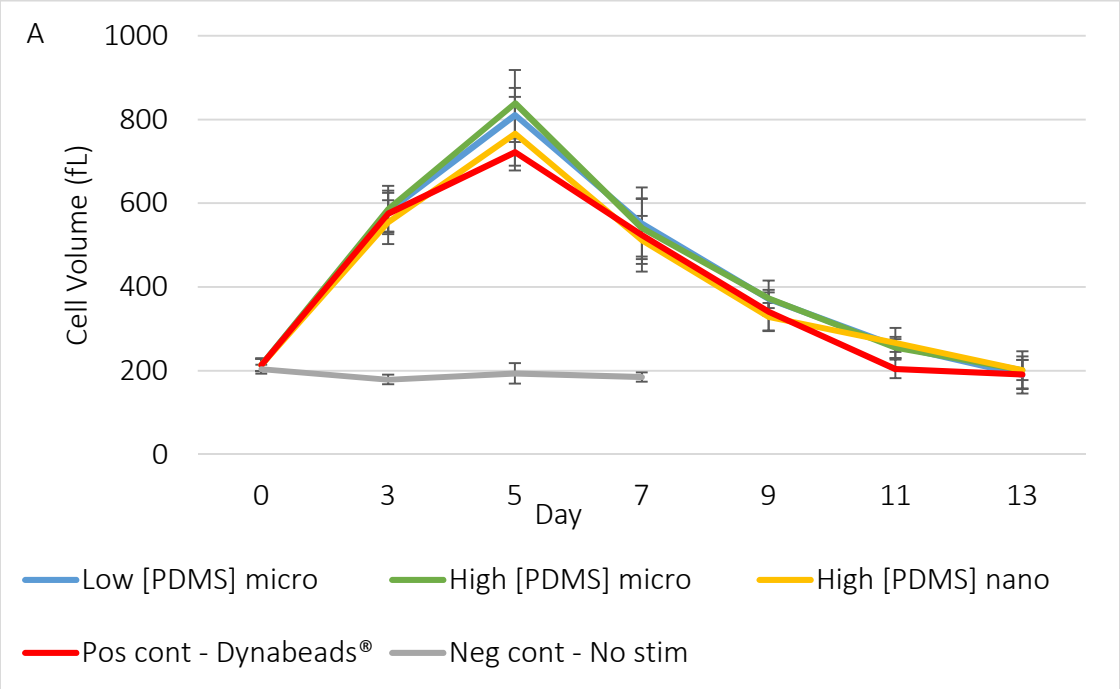

Figure 8: (A) Average cell volume (n = 4) from days 0-13 on select unaligned M4086 meshes. Cells were considered resting after average cell volume dropped below 400 fL.

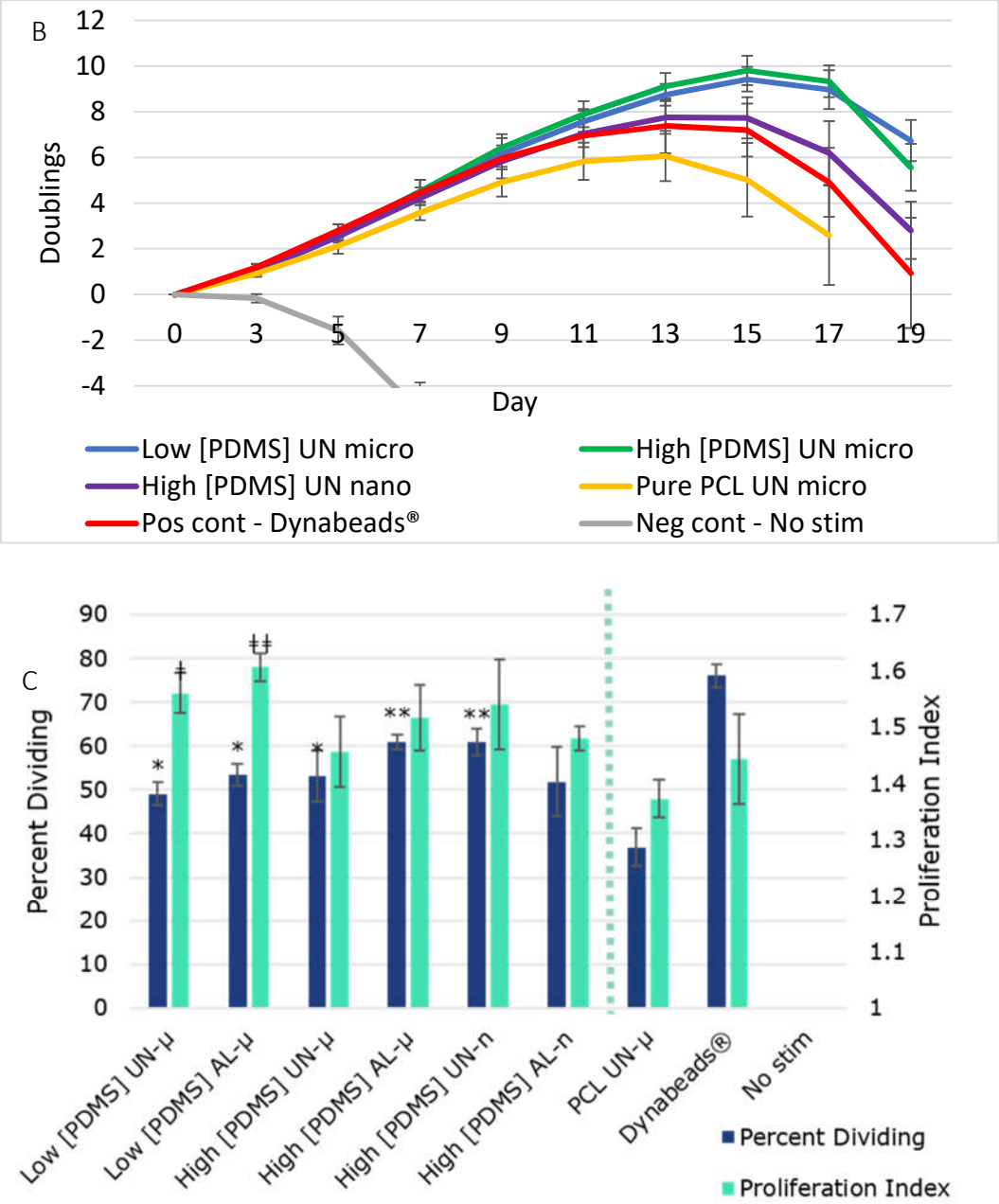

Figure 8 (continued): (B) Cell proliferation across days 0-19 (n = 8) on (UN)aligned meshes. (C) Cell activation level as quantified via %div and PI for expansions on (UN)aligned or (AL)igned meshes with (μ)scale or (n)anoscale fibers. All p-values are for one-way ANOVA. *, ǂ $p < 0.05$ compared to PCL, Dynabeads® respectively; **, ǂǂ $p < 0.01$ compared to PCL, Dynabeads®, respectively. All error bars mean ± standard deviation.

In each pair of unaligned and aligned meshes, unaligned meshes consistently outperformed the aligned ones in terms of population doublings. This may be attributed to the significantly higher fiber density and lower pore size as previously noted in the table in figure 5. This cramped structure was postulated to inhibit cell penetration into the mesh matrix and full leverage of the high surface area to volume ratio. To this end, fluorescent microscopy images of protein concentration revealed that nanoscale meshes had the lowest protein penetration of all meshes, with a strong protein signal lasting only approximately 12-15 μm into the mesh.

Cellular activation was quantified at day 3 through two different measurements: the number of cells entering primary division (%div), and the proliferative index (PI), herein defined as the average number of divisions an average cell has undergone and with a calculation formula as previously discussed. Although Dynabead®-expanded cells were observed to have a significantly higher %div, experimental mesh-expanded cells, particularly ones expanded on low [PDMS] meshes, were seen to have significantly higher PIs. Specifically, while Dynabeads® cultures attained anywhere from 19-35% higher %div than experimental mesh cultures, low [PDMS] mesh cultures outperformed Dynabeads by 0.1 to 0.2. This indicated that while PDMS/PCL meshes may slightly less conducive towards stimulating naïve T cells into primary division, those that do get stimulated become significantly more activated than their Dynabead®-activated counterparts. Notably, PI does not scale linearly, therefore, an n% increase in PI will correspond to a higher percentage of cells entering higher levels of division. Furthermore, experimental meshes demonstrated significantly higher values for both PI and %div than rigid control meshes, thus indicating that softer substrates may provide for better activation of naïve T cell populations. Additionally, microscale fibers were seen to yield slightly higher numbers of doublings than

nanoscale fibers. Due to this and the relative ease of making unaligned fibers compared to aligned fibers, studies performed herein will primarily focus on the use of microscale, unaligned PDMS/PCL meshes as the experimental substrates.

It should be noted that the higher %div reported for Dynabead®-cultured cells may be due in part to difficulty in separating stimulated cells from the underlying mesh. Currently, this is done via mechanical pipetting motions on day 3 of culture. Although we have observed cells to naturally detach from the mesh after four days of culture, cells were removed on day three in order to keep protocols consistent with the Dynabead® protocol, and cells that have penetrated the mesh further may still remain even after washing. Therefore, a more efficient removal method may lead to the release of more cells that have been induced into undergoing primary division but still maintain a high affinity for the mesh.

To further evaluate the functionality of mesh and bead-stimulated cells, cells were harvested from culture after returning to rest as measured by cell volume. The current model for adoptive immunotherapy has expansion facilities and bioreactors separate from the clinics themselves due to the high costs associated with setting up and maintaining these facilities: cells are harvested and frozen down prior to being transported between expansion facilities and clinics. In order to mirror the current model therefore, cells were frozen down and stored for at least one day in liquid nitrogen prior to being thawed and restimulated for functionality assays. Restimulation assays in $CD8^+$ cells revealed similar expression levels of CD107b, a surface marker for cytotoxicity, across both mesh and Dynabead®-expanded cells, with all groups exhibiting approximately 70-80% expression. Similarly, assays in $CD4^+$ cells for IFNγ secretion, a key cytokine for the activation of immune cells, showed a similar pattern, with no significant difference noted across experimental

or control groups at 75-85% expression (see figure 9A). It should be noted, however, that secondary stimulation appeared to be necessary to inducing our reported levels of cellular activation: cells that were harvested, frozen, thawed, but not restimulated only showed only 10-25% for both CD107b expression and IFNγ secretion across all groups, most of which can be attributed to background staining. This was not unexpected, as unstimulated, circulating memory T cell phenotypes do not become activated until seeing target antigen a second time.

Phenotypic assays likewise revealed a similarity in cell phenotype after restimulation, particularly in terms of central memory and naïve cells after cultures returned to rest. In general, all culture groups were observed to be primarily composed of central memory cells, with 60-80% of the population showing markers for both CD45RO and CCR7 (see figure 9B). As previously observed with CD107b expression and IFNγ secretion, restimulation was necessary to see this shift in cell phenotype, as without restimulation, only 20-40% of the population were observed to be central memory cells. Naïve cell populations on the other hand were observed to be a minority all throughout, although upon restimulation, populations tended to drop from 15-40% to 0-10%. This phenotypic distribution data coupled with the results of the restimulation assays confirm that while experimental meshes yield higher numbers of cells from the same starting population, the phenotypic profile remains constant and the level of cell activation upon restimulation remains unchanged. It should be noted that again, there was no significant differences observed between aligned and unaligned meshes of the same formulation.

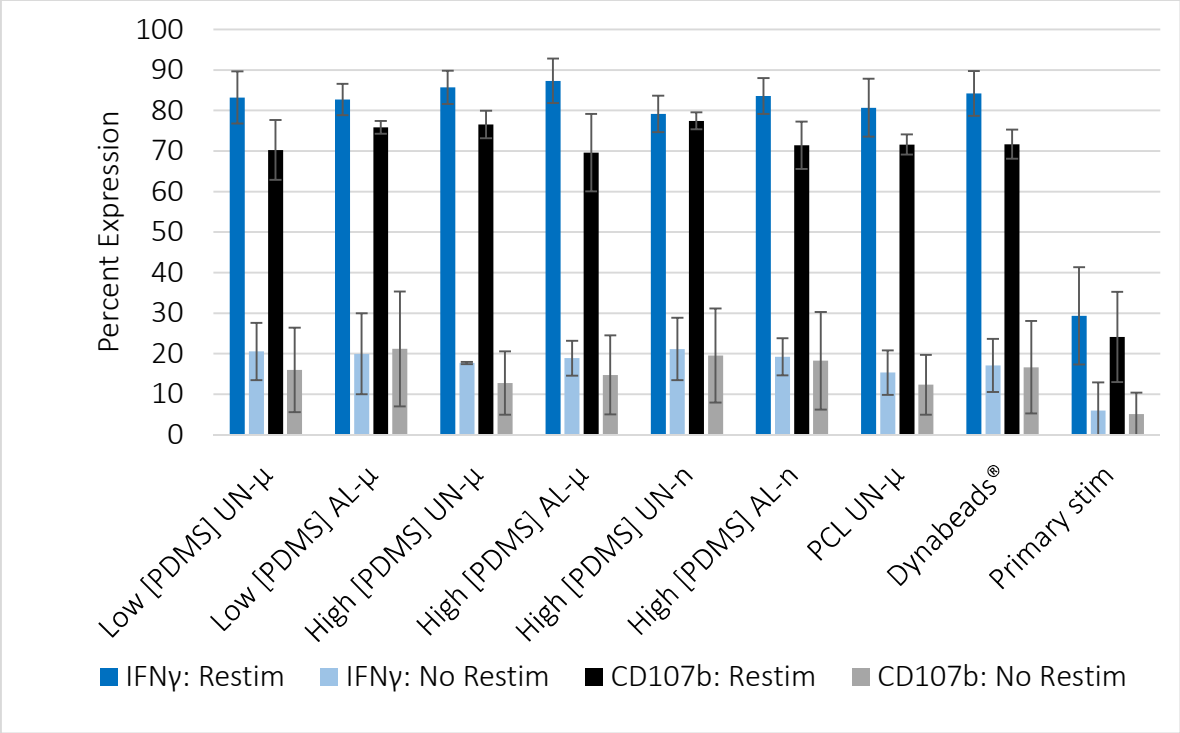

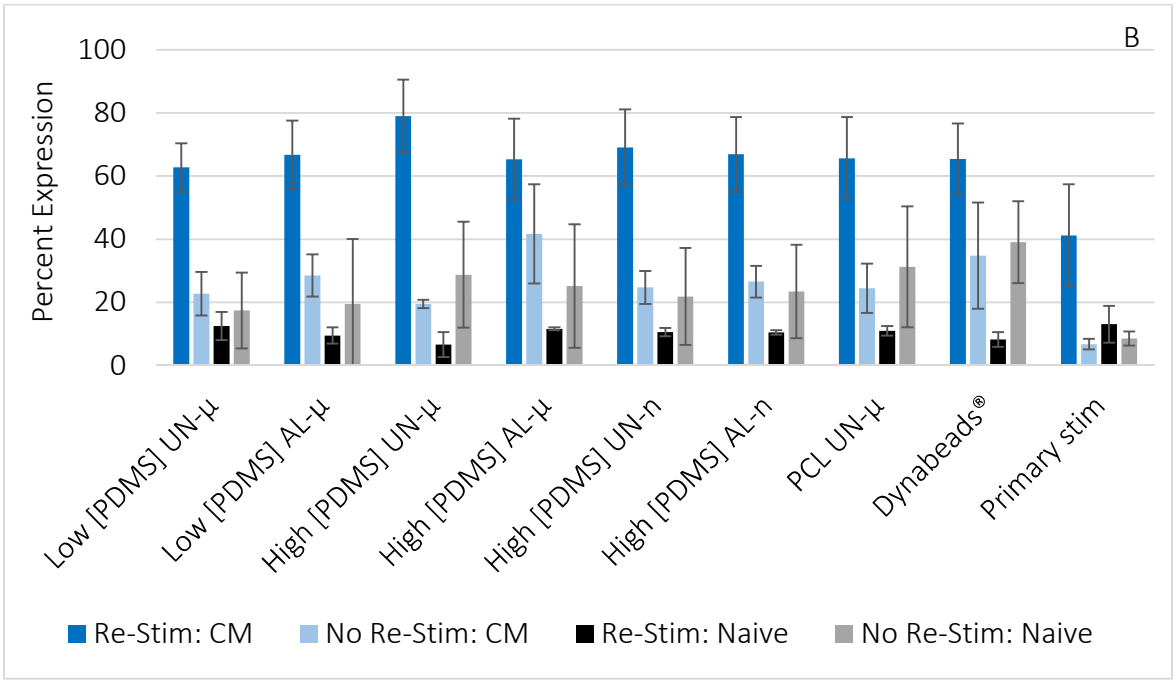

Figure 9: (A) IFNγ secretion and CD107b expression levels (n = 4) with and without restimulation. (B) Central memory (CM) and naïve cell populations with and without re-stimulation (n = 4). All error bars mean ± standard dev.

CLL patient cell expansions

Experiments that have been discussed up to this point have focused on the use of naïve T cells isolated from healthy human donors aged 18-64. However, patients that are best suited for ACT tend to be suffering from chronic illnesses. Therefore, in order to fully explore the functionality of the mesh platform, T cells isolated from CLL patients were expanded and evaluated for activation and proliferation. It should be noted that although a wide range of chronic illnesses can potentially be treated by ACT, CLL was chosen for this experiment due to its prevalence in prior studies on the uses of ACT. The progression of CLL can be best divided into different stages as described by the Rai classification or Binet classification schemes. Most commonly used in European countries, the Binet scale classifies patients by both the number of compromised lymph tissue groups, i.e., spleen, liver, and neck lymph nodes, and the rarity of erythrocytes and platelets in the blood. However, for this report we will be using the Rai staging system. Most commonly used in the United States, the Rai staging system breaks up patients into five categories from stage 0 (least severe) through 4 (most severe) inclusive.

The baseline threshold for CLL diagnosis is commonly taken to be monoclonal lymphocytosis, in which at least 5 000 monoclonal B cells per microliter of blood. In Rai stage zero, lymph nodes and lymph organs appear normal. However, as the Rai stage increases to 1 and 2, the lymph nodes, and the spleen become engorged, respectively. Rai stages 3 and 4 are subsequently characterized by additional anemia and thrombocytopenia, respectively, on top of the enlarged lymph organs. Only about 10-15% of all CLL patients are in stages 3 and 4, and furthermore, since the average age at diagnosis is 71 years in the United States, the immune systems of Rai stage 3 and 4 patients are particularly vulnerable[36] and may benefit from ACT. Common to patients of all Rai stages

however is the prevalence of exhausted T cell populations as seen through the expression of PD-1 on the surface of the cell. Notably, cell populations showing elevated levels of PD-1, coming from repeated stimulation of the adaptive immune system against overproduced non-functional B cells, have been shown to not be consistently expandable with the Dynabeads® platform.

Cell proliferation and activation experiments conducted with CLL patient-derived naïve T cells on low [PDMS], high [PDMS], pure PCL, and Dynabead® stimulating surfaces in the same manner as their healthy counterparts revealed a similar overall growth pattern in which cell populations that responded to treatment underwent a blasting phase followed by returning to rest, regardless of the rapidness of division. However, in certain populations, particularly those at higher Rai stages, this blasting phase was prolonged for longer and at lower intensities than observed in healthy cells, with some cultures blasting for up to 13 days but achieving lower levels of max doublings. Certain cell populations generally did not respond well to treatment: in one particular patient, low [PDMS] meshes achieving only 1.4 doublings, Dynabeads® achieving 0.81 doublings, and pure PCL meshes achieving 0.96 doublings. This was further echoed in low values of PI and %div, although these cultures, although the vast majority of cells died after day 3, a small, active population underwent division. This phenomenon was relatively uncommon: of the 24 patients reported in this thesis, only three patients were seen to exhibit low levels of cell proliferation across all substrates. Importantly, in all patients, regardless of expansion profile, a trend towards higher proliferation and activation on softer substrates within each Rai stage was observed. Additionally, maximum doubling levels were observed to drop across each Rai stage within the same substrate type (see figures 10A and B). Specifically, cells from Rai stage 0 patients were able to attain upwards of 6.39 $\pm$ 0.79 maximum doublings (approximately 83.86 times the starting population of cells) on low

[PDMS] meshes, a value that does not differ greatly from the expansion of healthy patient cells. As Rai stage increases, this value drops to 5.62 $\pm$ 0.24, 5.89 $\pm$ 0.96, and 4.84 $\pm$ 0.26 doublings in Rai stage 1, 2, and 3 patients respectively, and to just 3.09 with Rai stage 4 patients. Although a downward trend was not perfectly observed, due to the fact that average max doublings in Rai stage 2 patients is marginally higher than that in Rai stage 1 patients. Due to the small margin of difference and relatively low sample size (n = 5 and 6, respectively for Rai stages 1 and 2), this was attributed to experimental error. Notably, only five of the patients from our sampling were at Rai stages 3 and 4 at the time of blood withdrawal due to the rareness of these patients overall. Although the power of this study was hampered by this phenomenon, a trend towards lower levels of cell proliferation in higher Rai stages can nonetheless be observed. It should be noted that cells from healthy patients were expanded alongside CLL cells in these experiments in order to serve as controls. For both isolations from whole blood and frozen PBMCs, staining for CD3 post-isolation revealed a purity of over 93 percent (data not shown), thus indicating that these were indeed T cells that were being expanded.

This difference in maximum doublings became greater with increasing substrate rigidity: Rai stage 0 cells attained an average of 4.2 maximum doublings on Dynabeads®, compared to only 0.8 with Rai stage 4. Still, PDMS/PCL meshes outperformed Dynabeads® and PCL control meshes at every Rai stage, thus implying a higher level of cell proliferation for CLL patient-derived T cells on softer substrates. This of particular note in Rai stage 3 and 4 patients, where experimental meshes were observed to yield upwards of approximately 3.1 to 4.2 more doublings, or 8.5 to 18.3 times more cells than the clinical gold standard.

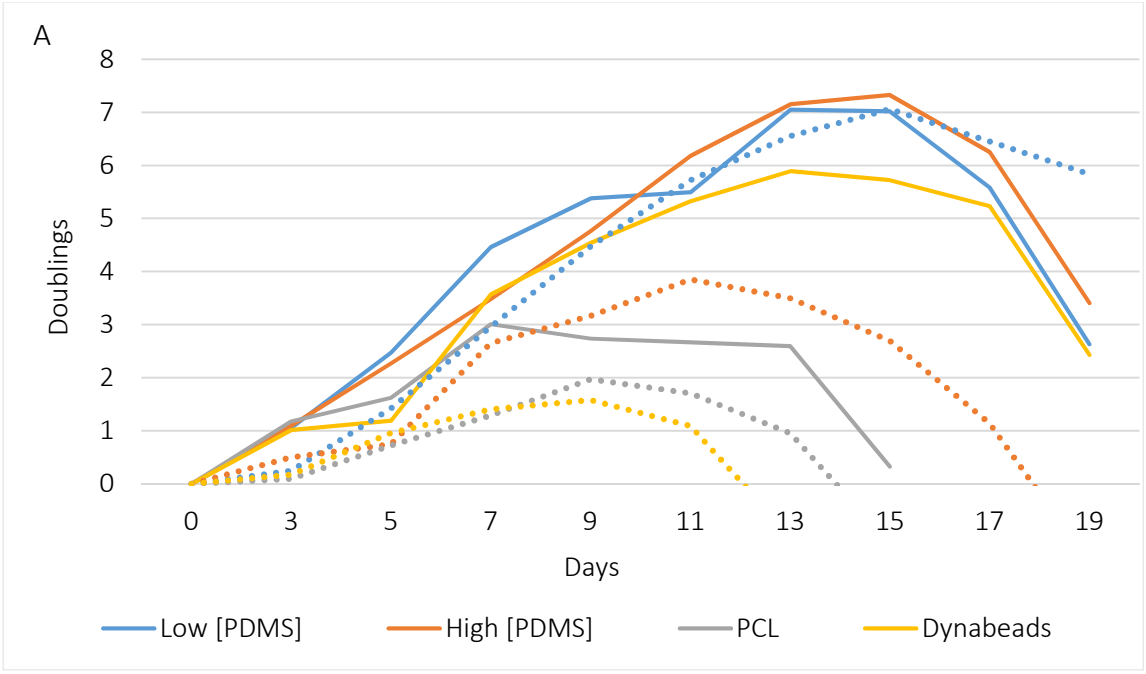

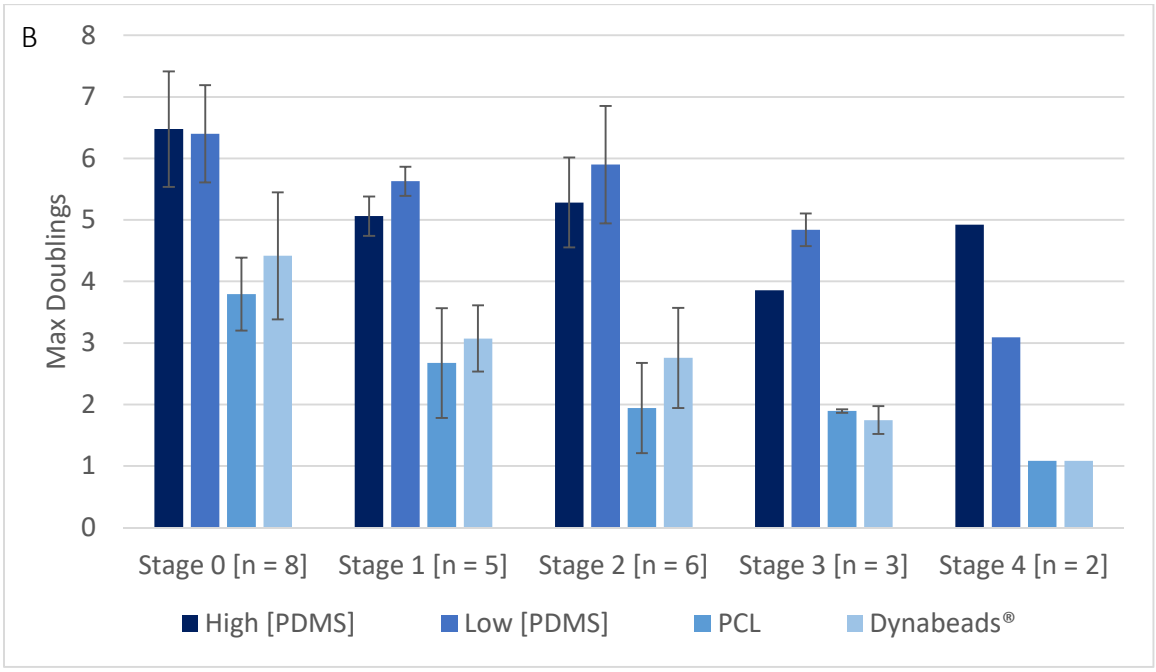

Figure 10: (A) CLL patient-derived T cell expansions. Solid lines denote Rai stage 0 and dashed lines denote Rai stage 3. (B) Maximum doublings for CLL expansions. Substrates are ordered from softest (dark) to most rigid (light). Stage 3 samples had n = 3 except for high [PDMS], where n = 2.

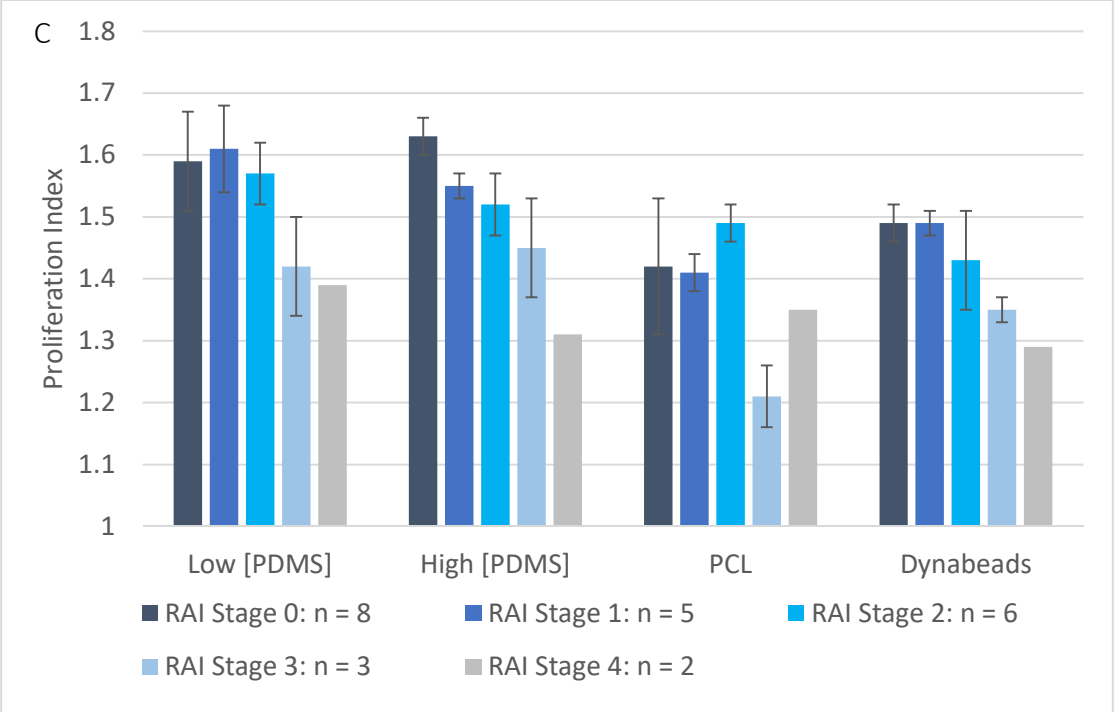

Figure 10 (continued): (C) PI for CLL expansions. All error bars mean ± standard dev.

However, significant variation was observed both between patients from different Rai stages, and between patients of the same Rai stage, as reflected in the error bars in figure 10. This level of patient to patient variability would inevitably be reduced by expanding more patient cells. This trend towards higher cell proliferation on softer substrates was mirrored in cellular activation, where PI levels were observed to reach upwards of 1.63 in Rai stage 0 cells on high [PDMS] meshes compared 1.49 on Dynabeads® (see figure 10C) Similarly, Rai stage 3 cells were observed to attain PI levels of approximately 1.42 on high [PDMS] meshes, compared to 1.20 and 1.35 on PCL meshes and Dynabeads®, respectively. Secondary stimulation assays for IFNγ secretion in $CD4^+$ cells and CD107b surface expression on $CD8^+$ cells again showed comparable activation levels for re-stimulated and non-re-stimulated cells to healthy cell expansion experiments (data not shown).

However, this level of variation may also imply that perhaps other factors or a combination of other factors are at play in determining how a CLL patient T cells respond to *ex vivo* stimulation. This is not of particular surprise due to the various differences in cell biology that are observed in CLL patients, such as genetic mutations and surface marker expression. Further discussion on this topic can be found in the conclusions and further directions section of this thesis. Ideally, a study would be performed evaluating the activation and proliferation of cells from a single CLL patient multiple times in order to evaluate intra-patient variability. Unfortunately, this was not practical in this experiment due to the limited quantities of blood and extremely limited quantities of PBMCs available from these patients, as well as the fragility of these cells. As patient schedules for bloodwork in the clinic are widely variable, patient deaths may occur, and patients may choose to move out of the region, we were not guaranteed that a patient would return to the clinic at a later time point. Additionally, treatment regiments for CLL, such as the use of monoclonal antibodies or other drugs, may have affected this study. Furthermore, depending on the severity of the disease, certain patients would only come to the clinic every half year or every full year. Nonetheless, in spite of these drawbacks, this section of our study indicates that experimental PDMS/PCL meshes hold significant promise for the *ex vivo* expansion of T cells from patients suffering from chronic illnesses such as CLL, and if further developed, can potentially become a driving force for furthering the adaptation of ACT in the clinical setting.

Results and Discussion: Specific Aim 2

Specific aim 2a: *Quantitative model for PDMS/PCL mesh rigidities*

Central to the notion of T cell mechanosensing is how a cell interacts with the underlying substrate. While we have actively demonstrated the correlation between cell activation, cell proliferation, and substrate rigidity, precise measurement of what the underlying mesh rigidity is required for full understanding of what forces the cell experiences. Bulk rigidity measurements (i.e., uniaxial tensile testers) are not ideal for full elucidation of this phenomenon due to the underlying fibrous geometry of the mesh itself. Furthermore, due to the geometry of the mesh, the rigidity that cells respond to may not be the local rigidity of the material itself, but deformations experienced on a more macroscopic scale. As previously discussed, back-of-the-envelope calculations using simple structural mechanics reveal that a single cell acting as a point force on a beam with single micron-diameter beam made of soft elastomeric material will produce significant beam deflections δ anywhere up to approximately 240 to 350 nm. Seeing as SEM images have revealed fiber diameters on experimental meshes to be approximately 1-2 µm in diameter, this deformation represents a significant 17 to 20% of the fiber diameter. Therefore, the overall perceived, or effective, Young's modulus E_{eff} of the mesh may very well be different than the Young's modulus of a slab of the mesh material, or even the local rigidity itself. As mentioned previously, this can be compared to climbing a rope ladder: while single hemp fibers are rigid to the touch, a person climbing said ladder will feel significant give and flexibility in the overall rope structure. A fibrous mesh also introduces various other factors not typically considered in traditional beam-bending mechanics such as the traction forces between individual fibers, the non-uniform lengths and

diameters of fiber segments, the supporting force of fibers below the top surface, and the adhesion forces stemming from of the nature of the material itself.

As of this writing, there has not yet been a fully studied, unifying model detailing the effective Young's modulus of single micron mesh fibers that takes these additional factors into consideration. Euler-Bernoulli theory presents itself as viable starting point however; such a model would be of particular use to this project as it would allow one to more precisely calculate how well the results of this experiment correspond to previous experiments detailing the effect of the rigidity of planar PDMS surfaces on T cell expansion. In other words, it could yield valuable insights into why the cells exhibited the behavior observed during expansion experiments, although the exact mechanisms of T cell force sensing, i.e., which proteins are involved, what traction forces are exerted, and what the signaling cascade is, are not yet fully studied and is currently being studied by this lab. Although the addition of PCL to the PDMS undoubtedly increases the material Young's modulus, the role of fiber geometry may indeed make the fiber appear less stiff than this figure. Therefore, we hypothesized that given a fixed material composition, one can formulate a model for the effective Young's modulus as a function of fiber geometry parameters such as length and radius via modifications performed on fundamental Euler-Bernoulli theory.

In order to accurately probe mesh rigidity at the nanometer scale, experiments in measuring mesh rigidity were conducted via AFM, which through a series of fixed complex equations and calculations can translate movement of a mounted tip into values for local Young's modulus, tip adhesion, and surface deflection, among other values. As previous experiments have indicated, AFM tip geometry may have a significant impact on the topological maps received. Although a naïve T cell can be roughly approximated as a 7 μm diameter sphere, spherical AFM tips of that

size may readily get trapped in the mesh pores themselves, thus rendering AFM imaging impractical. Furthermore, tip diameter is inversely proportional to AFM image resolution, as one can probe more points per unit area with a smaller tip. Additionally, tip cantilever should also be taken into consideration, as stiffer cantilevers ($k > 10$ N/m) may not produce sufficient deflection when probing softer surface. On the other hand, using a soft cantilever on a rigid surface may not produce sufficient material deformation to generate an accurate topological image or measure mechanical properties. As an AFM is typically designed for analysis of a wide range of materials, ranging from rigidities single digit pascals to gigapascals, a wide range of cantilever stiffness levels are available. With this in mind, for this project, sharp AFM tips with diameters between 5 and 17 nm with low cantilever spring constants for greatest measurement resolution and accuracy (cone, $d < 30$ nm, $k = 0.4$ N/m), were used. Notably, all AFM experiments were performed in air. Although cells are expanded on the mesh in an aqueous environment, AFM experiments in liquid may not yield significant difference in measured values. This is particularly true of PDMS/PCL meshes since both materials are hydrophobic, do not readily degrade in water over the course of several weeks, and do not swell or shrink significantly, such as in the case of hydrogel systems. Peak force setpoint (pFS) levels in this experiment, defined as the maximum force level exerted on the substrate, were kept in the single digit to tens of nN range in order to mirror forces exerted by cells on surfaces. Tapping mode was used in lieu of contact mode in order to prevent tip damage and degradation, and in order to focus on our best performing meshes, this experiment analyzed unaligned micro PDMS/PCL meshes in both low [PDMS] and high [PDMS] formulations. Additionally, microscale pure PCL meshes were analyzed due to their previous use as controls in the expansion experiments, and calibration was performed with the softest substrate available, a 2.5 MPa PDMS slab.

Initial topological AFM images supported fiber geometries previously derived from SEM images. With this technique, high [PDMS] and low [PDMS] meshes were revealed to have rigidities ranging from 640 ± 140 kPa to 1.24 ± 0.32 MPa, respectively, compared to 46.4 ± 14.8 MPa for PCL meshes (see figure 11). While Dynabeads® were not measured for this experiment, rigidities were estimated to be approximately 1.9-2.9 GPa according to the literature values for poly(styrene). Due to the lack of sudden rigidity shifts or extraneous beading in the rigidity and topographical mapping, respectively, fibers were concluded to be homogeneous and devoid of PDMS or PCL-rich regions: phase separation of precursor polymers was not observed.

In addition to high [PDMS], low [PDMS], and PCL meshes, aged low [PDMS] meshes were analyzed in order to evaluate what, if any, changes in rigidity may occur at prolonged timescales. This was of particular interest to us for further development of this mesh as a viable commercial platform, as the shelf life of products need to be taken into consideration prior to marketing: an increase in rigidity over time would imply that meshes may not retain their functionality over longer timescales. In this experiment, low [PDMS] meshes aged nine months at room temperature in a dark location were used as old low [PDMS] meshes. Interestingly, aged experimental meshes were seen to exhibit slightly higher rigidities than their freshly spun counterparts: old low [PDMS] meshes were found to have average fiber rigidities of 14.7 ± 5.06 MPa, amounting to an almost ten-fold increase in stiffness compared to a freshly spun low [PDMS] mesh. While expansions have not yet been carried out on aged PDMS/PCL meshes in order to evaluate any decrease in cell stimulation efficacy, this may have further implications for clinical adaptation of this technology due to the time-dependent nature of measured rigidity

One notable phenomenon observed when evaluating mesh rigidities was how fiber position qualitatively appeared to have an effect on measured rigidity. This is demonstrated in figure 11A, where areas of strong mutual fiber support (i.e., the upper right hand corner of the high [PDMS] image) appear significantly more rigid (white) than areas where fibers are string between two focal points (i.e., center of the vertical transverse fiber in the same image). A similar phenomenon can be seen in figure 11B, in which areas where fibers are bundled on top of each other (i.e., the middle of the vertical fiber cluster) appear to have higher rigidities than both the surrounding fibers and areas of the same fiber that are further away from the cluster

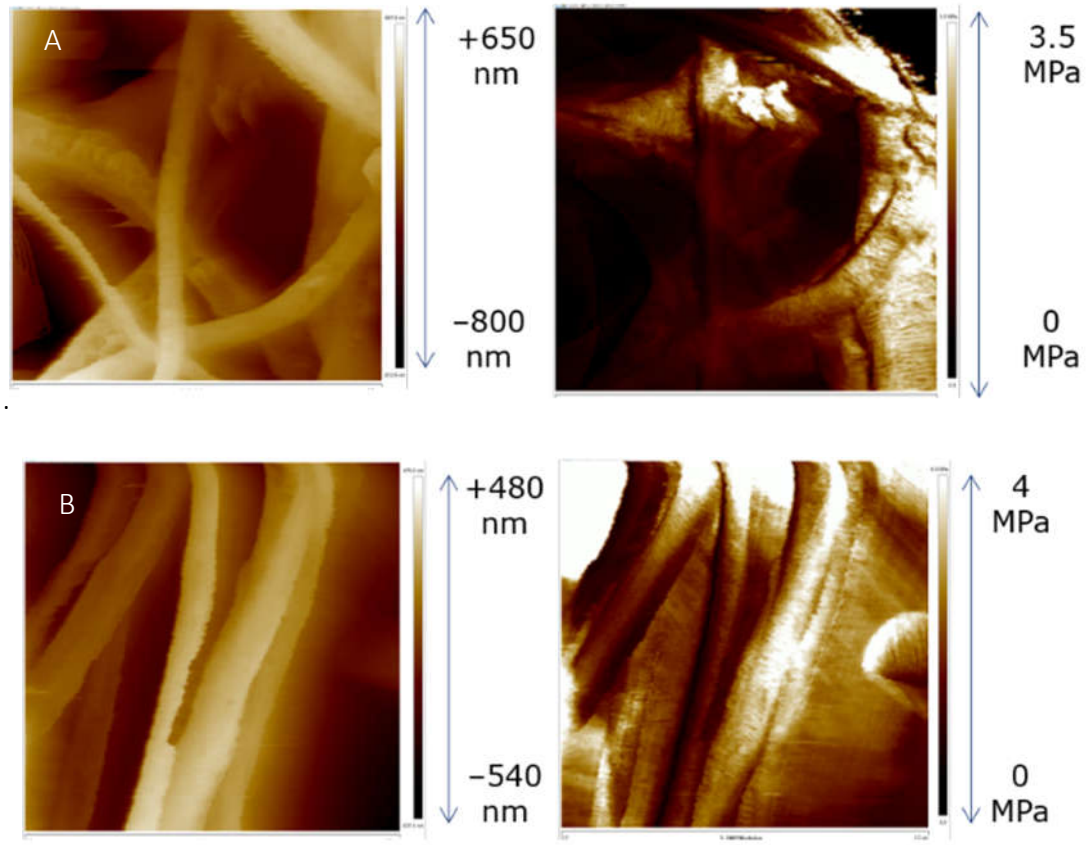

Figure 11: Topographical (left) and rigidity mapping (right) for (A) high [PDMS] and (B) low [PDMS] meshes. All images 2 µm x 2 µm.

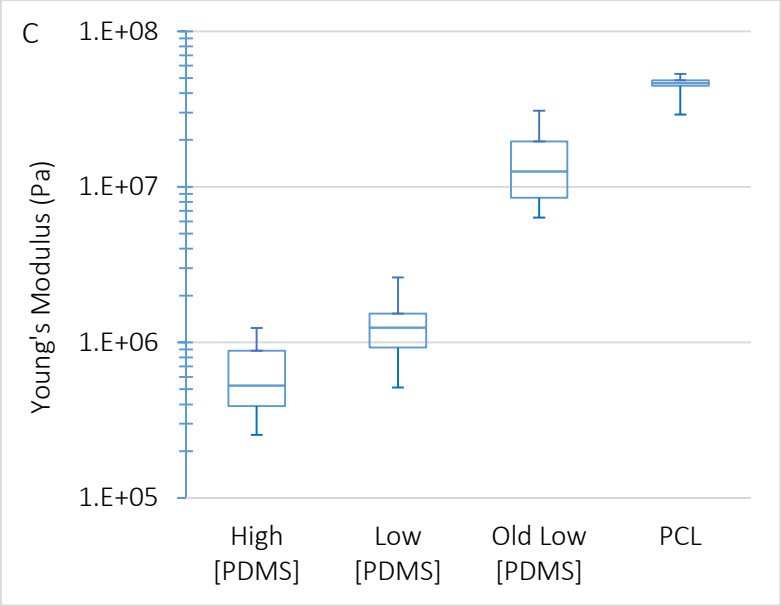

Figure 11 (continued): (C) Average measured fiber rigidity for high, low, and old M4086 meshes, along with PCL. Figures represent averages over n = 6 scans.

As the applied AFM tip force was kept in the single digit to tens of nN range for initial rigidity experiments, this data implied that fibers were responding to nanoscale forces of this magnitude. In order to further investigate how applied nanoscale forces affect rigidity, follow-up experiments focused on modulating the peak force set-point (pFS), or the maximum allowable tip indentation force from the AFM, and observing any effect on measured rigidity. This appeared to be indeed the case: as seen in figure 10, as one raised the pFS from 4 to 40 nN on a single aged low [PDMS] mesh the average fiber rigidity was seen to spike from 13.38 ± 0.57 MPa to 32.16 ± 1.94 MPa. A similar phenomenon was also observed with both aged high [PDMS] and pure PCL meshes, thus indicating that this phenomenon may be more characteristic of the substrate geometry and synthesis process rather than the bulk material itself. As the pFS was increased, a quadratic relationship between E and pFS was observed (see fig. 10B), thus further implying that simple beam bending may in fact be at play here. It should also be noted that subsequent decrease of the

pFS from 40 nN back to 10 or 4 nN reflected lower measured rigidities. This reversibility implied that the increase in measured rigidity was not the result of multiple scans over the same line, but was primarily due to the pFS.

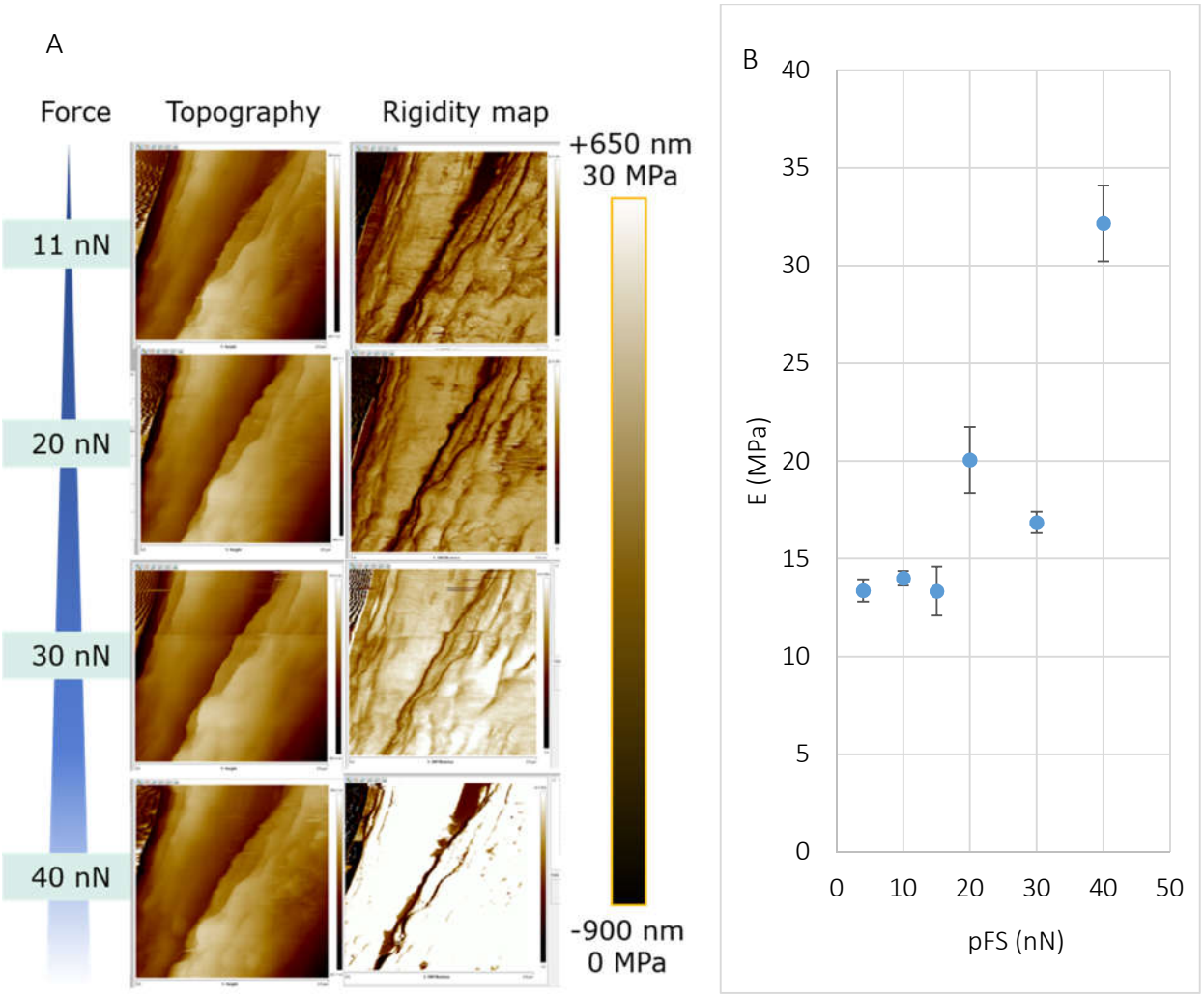

Figure 12: (A) Rigidity dependence on pFS for a single aged low [PDMS] mesh. All images 2 µm x 2 µm. (B) Measured rigidities in aged low [PDMS] mesh as a function of pFS. Error bars mean ± standard deviation (n = 12).

C

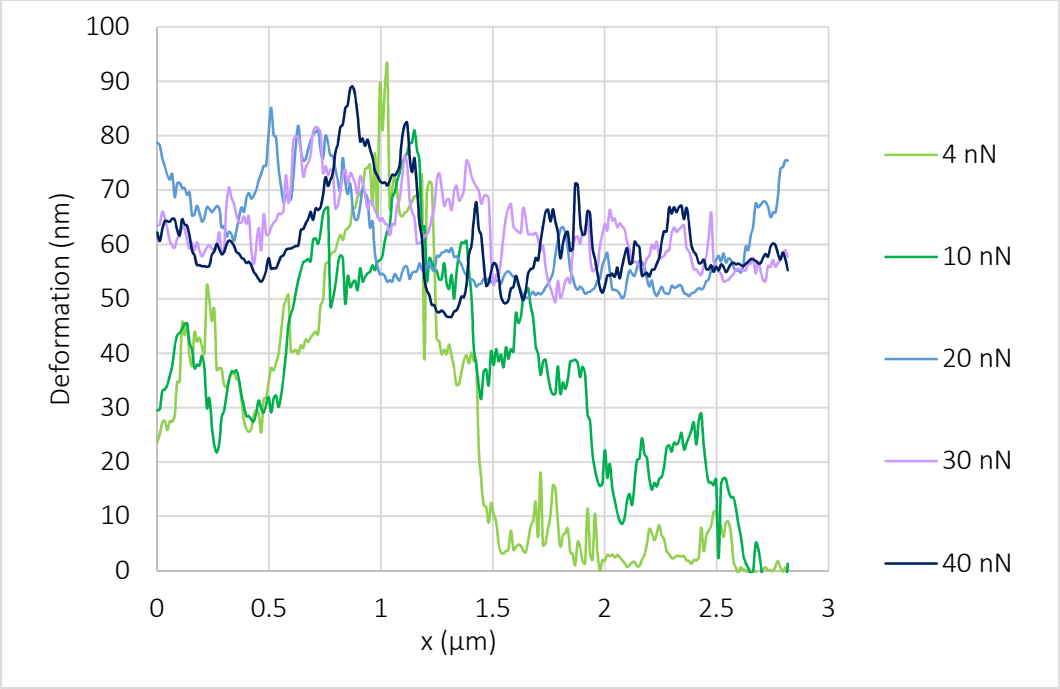

Figure 12 (continued): (C) Substrate deformation as a function of distance and pFS along identical paths on a single aged low [PDMS] fiber. Lighter lines denote lower pFS values.

In an ideal Hertzian model, substrate deformation, herein defined as the vertical distance moved by a single point on the mesh upon probing with the tip, would be zero as there is a perfectly elastic interaction between tip and substrate[37]. Substrate deformation was observed in this case to at points be approximately 90 nm, or approximately 7.5% the average fiber diameter, thus indicating again that a typical Hertzian contact model is not ideal for analyzing the surface of these meshes. Substrate deformation was also seen to vary with applied force: as one increased the pFS from 4-40 nN, substrate deformation was seen to steadily increase along the same path. Reverting to a lower pFS after scanning at a high pFS once again showed a similar substrate deformation curve as previously measured, thus again indicating that due to the reversible nature of this phenomenon, the tapping force is most likely the primary factor at play.

As a result of experiments on the effect of pFS on AFM-reported rigidity, deformation was postulated to be a function of applied force $\delta(F)$ composed of two primary components: Hertzian contributions, in which δ scales with the square root of applied force, and force contributions from the cantilever beam motion itself, in which δ scales linearly with F. This is notably different than standard AFM models, in which Hertzian contributions are dominant in δ. Therefore, we hypothesized that a more accurate function of $\delta(F)$ would take the following form, where a, b, and c are constants:

$$\delta_{real} = aF + b\sqrt{F} + c$$

Ideally, the linear offset c would be zero, however, due to experimental error, this will almost certainly not be the case. The is also notably different from standard Hertzian AFM models in which $\delta(F) = b\sqrt{F} + c$, i.e., where cantilever contributions are not considered.

In order to determine the mesh-specific constants a, b, and c, the average deformation at fixed pFS values were calculated. This was done by taking repetitive scans of the same mesh region and calculating the average fiber deformation in z (that is, parallel to the axis of AFM tip indentation), and performing curve fitting to both the classic Hertzian model as well as our cantilever-inclusive model. Percent reduction in the sum of residual squares between the data points and the fitted curve $\Sigma(R^2)$ were then calculated in order to quantitatively determine how accuracy was gained by the addition of the cantilever term. As seen in figure 13, the addition of the cantilever term did increase the deformation model accuracy in freshly spun low and high [PDMS] meshes, although this difference was minute and not considered statistically significant as determined by the Wald F-test. However, the opposite was observed for pure PCL and old low [PDMS] meshes, with a 26.5%

($p < 0.05$, Wald F-test) and a 30.1% increase in accuracy ($p < 0.01$), respectively. This discrepancy between the increase in accuracy between softer and stiffer meshes was largely in part due to the wide spread of deformation values at pFS = 20 nN, which produced substantially larger values for $\Sigma(R^2)$.

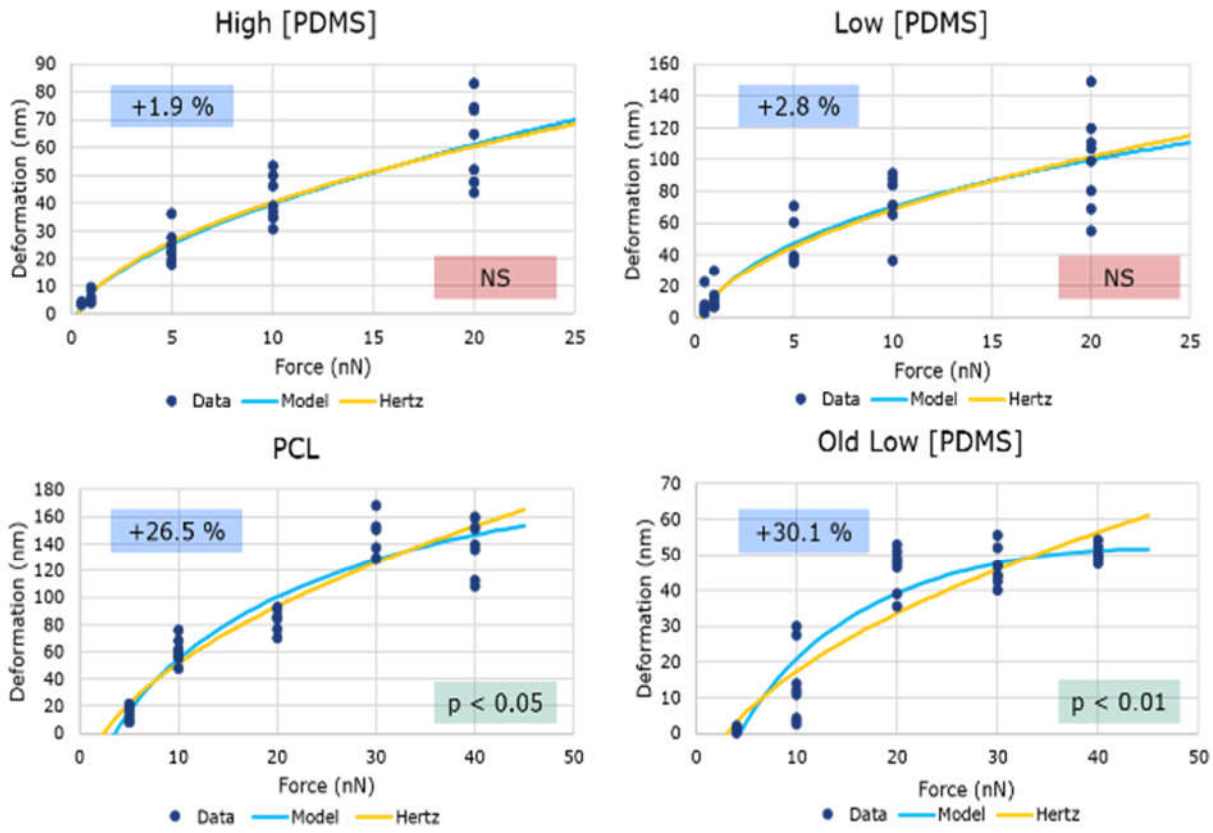

Figure 13: Hertzian (yellow) versus combined cantilever-Hertzian models (blue) for $\delta(F)$. Percentages represent the decrease in $\Sigma(R^2)$ by going from Hertz to combined cantilever-Hertz model. p-values were calculated by the Wald F-test.

Coupling with basic Euler-Bernoulli theory allowed for the calculation of E_{eff} given a set pFS:

$$E_{eff} = \frac{4L^3F}{3\pi r^4 \delta_{real}} = \frac{4L^3F}{3\pi r^4 \left(aF + b\sqrt{F} + c\right)}$$

This provided a rudimentary model for effective Young's modulus and allowed for a secondary calculation of E_{eff} for meshes. F in this case was taken to be 10 nN due to its proximity to the weight of a cell given $g \approx 10\frac{m}{s^2}$. Results using this mode of calculation more closely reflected expected values, with low [PDMS], high [PDMS], and PCL meshes yielding E_{eff} values of 294 $\pm$ 61 kPa, 251 $\pm$ 81 kPa, and 1.58 $\pm$ 0.21 MPa, respectively (see figure 14, dark blue columns). Although these more closely matched expected values for E_{eff} than with those in figure 11C, these figures were nonetheless slightly higher than expected, thus indicating that further modifications on Euler-Bernoulli theory may increase the accuracy of our model.

Notably, as E_{eff} is a function of F, it can be broken down into its cantilever ($\delta = aF + 0.5c$) and Hertzian ($\delta = b\sqrt{F} + 0.5c$) constituents. Analysis of the resulting decomposition strongly indicated that cantilever forces dominate the equation, especially at lower rigidities. As seen in figure 14 (green columns), cantilever contributions composed approximately 82.2%, 86.4, and 69.7% of the overall E_{eff} value for low [PDMS], high [PDMS], and PCL meshes respectively. This effectively indicated that as cantilever forces dominated, cells are sensing more macroscopic rather than local, microscopic forces on the mesh.

In order to expand upon this model and obtain a function of E_{eff} in terms of geometric parameters L and r, we first reconstructed the equation for E_{eff} to separate the Hertzian and cantilever components, while simultaneously applying Euler-Bernoulli theory to beam deflection. That is, given $\delta(x)$ as:

$$\delta(x) = \frac{Fx(L^2 - x^2)^{3/2}}{9\sqrt{3}LEI} \qquad I = \frac{\pi r^4}{4}$$

A

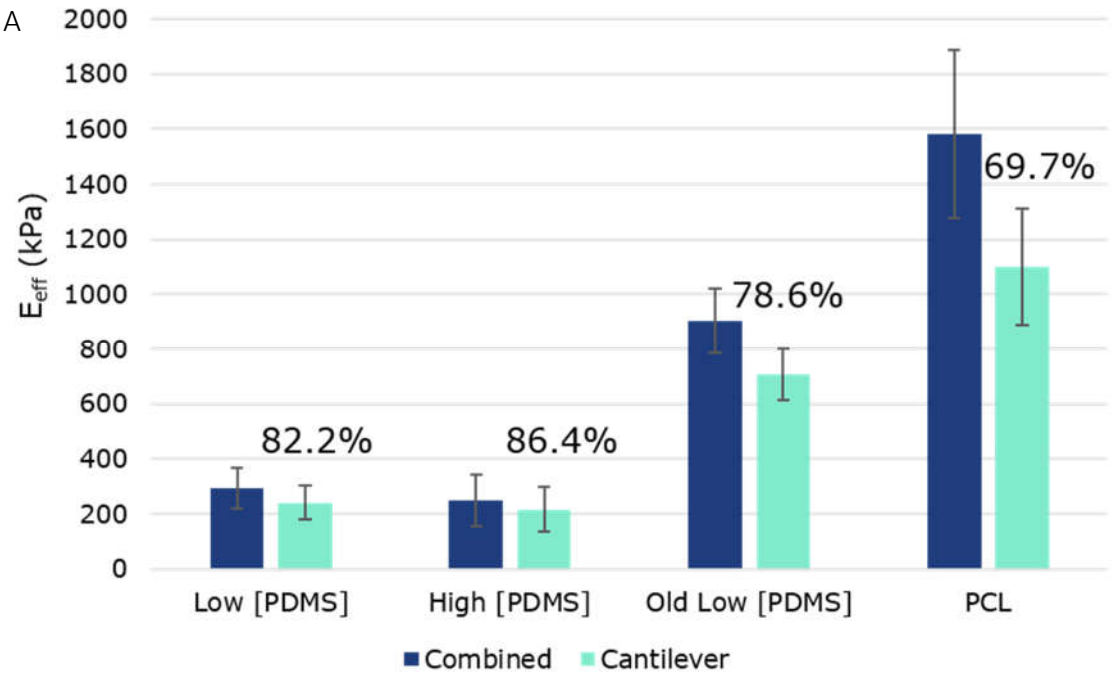

B

Results				
Mesh type	E_{eff} (Pa)	Cantilever	Cantilever fraction	S. dev
Low [PDMS]	294.1	241.7	0.822	61.3
High [PDMS]	250.9	216.7	0.864	80.5
Old low [PDMS]	903.0	709.4	0.786	93.7
PCL	1581.8	1101.9	0.697	212.4

Figure 14: (A) E_{eff} as calculated by basic modification of Euler-Bernoulli theory via $\delta_{real}(F)$. Error bars represent mean $\pm$ standard deviation, n = 5. (B) E_{eff} and corresponding cantilever contributions. Standard deviations n = 5 with respect to E_{eff}.

Effective Young's modulus thus became the following:

$$E_{eff}(x) = \frac{4L^3F}{3\pi r^4\delta(x)} + b\sqrt{F} + c$$

Although $E_{eff}(x)$ as written provides a reasonable estimate of effective Young's modulus, it is still a function of x. Ideally, a model would provide an overall estimate for the average effective Young's modulus for an entire mesh. To make this shift, $\delta(x)$ was approximated as $\bar{\delta}$ by determining the average distance between any one point on the mesh and a fiber node via SEM images and acquiring the value of E, the Young's modulus of the bulk material. To this end, slabs of low [PDMS] were synthesized via direct casting onto glass coverslips and subjected to AFM analysis as described previously. Although values for E of the casted slab varied, rigidities were found to be approximately 2.11 $\pm$ 0.84 MPa (n = 8 sample areas). The equation for deformation thus was reduced to a function of F, which, once placed back in the equation for E_{eff}, became independent of pFS. Since the Hertzian contribution was negligible for softer meshes (less than 20%) a reduced, simplified version of E_{eff} was obtained:

$$\bar{\delta} \approx \delta(\bar{x}) \;\rightarrow\; E_{eff}(r, L) = \frac{4L^3F}{3\pi r^4 \bar{\delta}} + c$$

Notably, the absolute value of the offset value c was found to be less than 25 kPa for low and high [PDMS], while values reached as high as 107 kPa for PCL meshes. Ideally, these values would be zero, thus indicating that our model was not a perfect predictor of E_{eff}. However, the lack of E_{eff} dependence on F was particularly beneficial since given a set material composition and relatively small exerted forces by the cell, effective rigidity should not be dependent upon probing force

While this model does provide a reasonable estimate, there are multiple factors that were not considered, including but not limited to tip adhesion, fiber-fiber traction forces, slippage, and peak force error. Future models may indeed analyze the contributions from these forces, however, for

the purposes of this study, these contributions were considered to be negligible compared to macroscopic beam bending deformations.

Specific aim 2b: *Verification of quantitative model for PDMS/PCL mesh rigidities*

Our aforementioned derived model allows us to estimate the effective Young's modulus for a mesh as a function of r, and L, given a fixed bulk material Young's modulus E. Notably, the majority of the value of E_{eff} came from was from the cantilever force contribution: this indicated that it is the macroscopic beam bending motion that cells primarily responded to, not local microscopic forces driven by the rigidity of the material itself. Therefore, given an array of different meshes constant materials composition but L, one can effectively calculate E_{eff} and perform the associated cell expansion as detailed in specific aim 1 of this report. For this segment, meshes with E_{eff} in the 10 – 500 kPa range were targeted in order to provide suitable comparison to the planar surfaces synthesized by O'Connor *et al*.

In order to validate our model, a series of meshes with differing values of average fiber radius r and average inter-node fiber length L were synthesized and the values for E_{eff} calculated. The low [PDMS] formulation was chosen for this final experiment due to its lower spinning time and more stable spinning process than its high [PDMS] counterpart. The formulation used in specific aim 1 of this report was used to create fresh low [PDMS] meshes as a starting point (herein termed mesh A); from here, electrospinning parameters, such as working distance, accelerating voltage, and spin rate were modulated in order to produce mesh variants. The resulting original mesh formulation was observed to have fiber diameter 2.28 $\pm$ 0.46 µm, while subsequent variations yielded fiber diameters of 1.82 $\pm$ 0.33 µm, 1.27 $\pm$ 0.28 µm, 0.55 $\pm$ 0.10 µm, and 9.39 $\pm$ 1.82 µm,

herein termed meshes B, C, D, and E, respectively (see figure 15). Resulting values for E_{eff} ranged from 61.9 ± 8.4 kPa and 29.7 ± 3.5 kPa in meshes A and B, respectively, to upwards of 387.8 ± 34.3 kPa in mesh D. Although mesh E had the highest fiber diameter at almost 10 µm, its E_{eff} is lower than that for mesh D primarily due to its larger fiber lengths. Mesh D on the other hand appeared stiffer despite having the smallest fiber diameter of this set due to its very short fiber length.

A

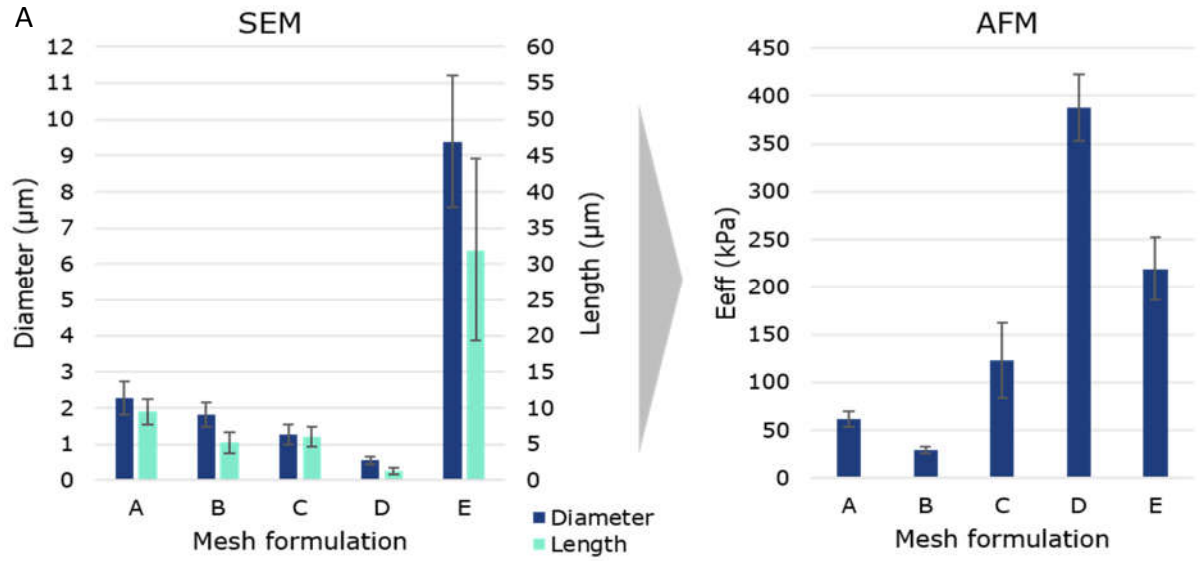

B

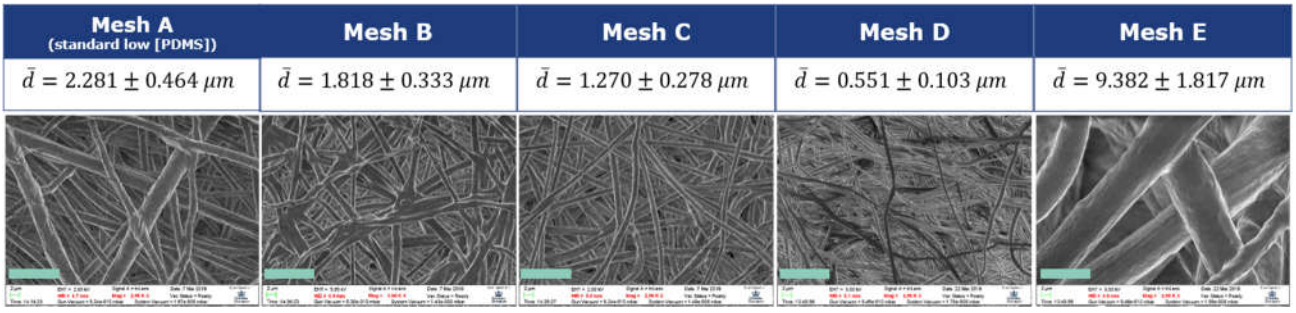

Figure 15: (A) Fiber diameters and average inter-nodal fiber length for meshes A through E (left) and resulting E_{eff} from model calculations (right). Values are mean ± standard deviation with n = 3. (B) SEM images of meshes A through E. All images taken at 2000x magnification, scale bar = 10 µm.

Meshes were subsequently mounted, coated with activating antibodies, and used as expansion substrates for naïve T cells derived from healthy donors as described in specific aim 1 in conjunction with Dynabead® controls. Expansion profiles once again reflected profiles observed with healthy donor cells as in specific aim 1, where cultures underwent an initial blasting phase for seven to nine days as tracked by cell volume before returning to rest. Importantly, the two softest meshes, A and B, ($E_{eff} \approx$ 60 and 30 kPa, respectively) were observed to yield the highest number of maximum doublings at 6.63 $\pm$ 0.34 and 6.67 $\pm$ 1.27 doublings, respectively. In contrast, the stiffest mesh, D, ($E_{eff} \approx$ 390 kPa) yielded 4.17 $\pm$ 0.42 doublings (see figure 16). This may again be in part due to its dense fiber structure, however, its geometric parameters yielded a much higher rigidity than its softer mesh counterparts. In addition, PI and %div data for meshes A through E varied from 1.47 to 1.72 and from 44.2% to 68.1%, respectively; these values were not seen to deviate significantly from those acquired from the previously run healthy donor expansions (data not shown). Following completion of primary blasting phase, cells were again harvested, frozen down, and subjected to restimulation assays for IFNγ secretion in $CD4^+$ cells and CD107b expression levels on $CD8^+$ cells. Restimulation assays yielded the same pattern as previous expansions with healthy donors, in which secretion and expression levels were not found to vary significantly (α = 0.05, n = 3, ANOVA) across all mesh types, thus indicating that cells retained comparable functionality as the Dynabeads® platform (see figure 16B).

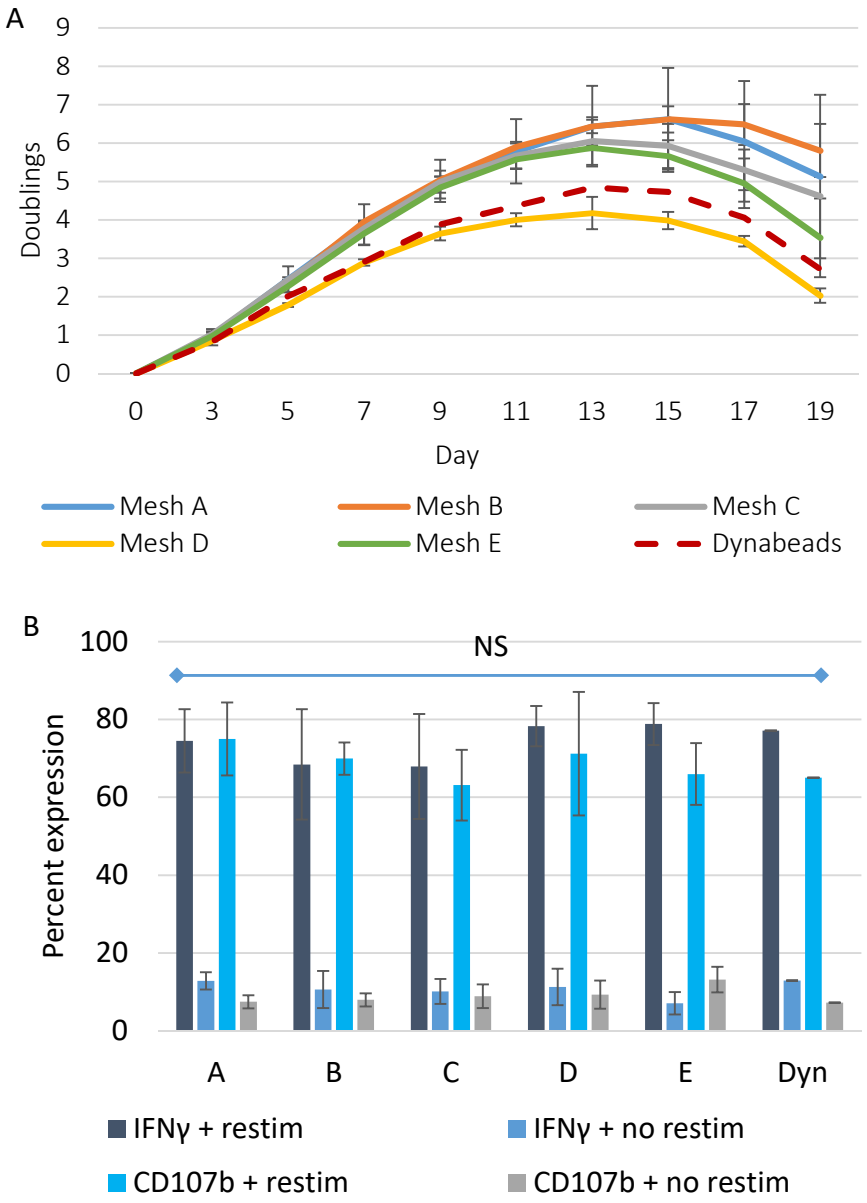

Figure 16: (A) Expansion profiles for meshes A through E. All mesh types n = 3 except for Dynabeads® (n = 1). (B) Restimulation experiment results for meshes A through E. All error bars represent mean ± standard dev, $\alpha = 0.05$).

This section of the report served as a validation for our previously formulated model. Notably, expansion curves as qualitatively measured by overall shape and quantitatively measured by

maximum doublings for the softest meshes, A and B, were comparable to those achieved by the 1:5 planar PDMS formulation synthesized by O'Connor *et al*, in which surfaces of rigidities of approximately 50-110 kPa were found to yield approximately 6.6 maximum doublings from a starting population of 1 million T cells in the same culture conditions. Although other aforementioned factors may still play a role in determining the true value of E_{eff} for microfibrous PDMS/PCL meshes, this analysis indicates that this model may be viable as a first approximation of E_{eff}.

In summary, specific aim 2 has seen the development of a quantitative model for the effective Young's modulus E_{eff} as a function of materials synthesis parameters L, the inter-nodal fiber length and r, the fiber radius, through a combined AFM and SEM-based study, as well as drawing upon the fundamental mechanics of beam bending as found in Euler-Bernoulli theory. Validation of this model via the expansion of human T cells as previously done in specific aim 1 and previous work by O'Connor *et al* indicate that this model provides a reasonable estimate of E_{eff} for fibrous meshes with set bulk material properties.

Conclusions and Future Directions

Summary and conclusions

Our motivation in developing the mesh platform described in this report was twofold. The primary goal is to improve upon the potential safety concerns in the use of the Dynabead® platform by having a single continuous substrate for ease of removal and lack of activating antibody being transfused into the patient along with the cell product while still maintaining a high surface area to volume ratio. In addition, our secondary goal was to engineer this platform to effectively allow for the leveraging of T cell based mechanosensing, a phenomenon previously demonstrated by our lab through observed trends towards higher levels of cell proliferation and IL-2 secretion on softer substrates.

Experiments conducted in this report have indicated that there is indeed a correlation between surface rigidity, cell activation, and cell proliferation in healthy patient-derived naïve human T cells. As evidenced by our experiments, cells are indeed penetrating into and becoming activated by the PDMS/PCL meshes. More importantly however is the trend, in which meshes made of the softest material achieved anywhere from two to approximately four more doublings from the same starting population as the clinical gold standard while maintaining comparable levels of cell activation, as measured by $CD4^+$ cytokine secretion and cytotoxic $CD8^+$ surface protein expression, and phenotypic distribution. Similar trends were also observed in cell volume progression, indicating comparable growth trends and blasting phases between cell populations. The first section of this report therefore indicated that the leveraging of T cell mechanosensing can indeed be achieved through the use of fibrous PDMS/PCL meshes with micron-scale geometries, thus

proving our original hypothesis correct. This is of particular importance in CLL patient cells, as the expansion of exhausted (PD-1^{high}) cell populations remains an active challenge in the full realization and clinical adaptation of adoptive cell transfer.

Central to the observations seen in this experiment was the ability to effectively tune fiber geometries in order to synthesize a platform with features that mimic the *in vivo* environment of the cortical and medullary thymus where T cells undergo final maturation. Our strategy in using PDMS, a non-toxic polymer approved by the FDA for use in medical devices, as the underlying material was largely due to its ease in rigidity modulation: by altering the base to crosslinker ratio, one is able to generate various substrates with different rigidities. In order to synthesize meshes via electrospinning, the addition of PCL was necessary in order to form a stable polymer feed with suitable viscosity. This effectively allowed for the synthesis of a series of meshes with microscale fibers and pores with diameters on the order of 1-2 µm and 9-12 µm, respectively as confirmed by SEM. This was of particular importance to us as it was hypothesized that these dimensions would promote cell migration into the mesh and fully leverage the high surface area to volume ratio of our construct. This was later confirmed via fluorescence microscopy: cellular actin staining coupled with mesh fiber staining revealed cells burrowing into the mesh and clinging onto fibers coated with agonists to CD3. While the precise mechanism and traction forces for T cell adhesion are still subjects of active research, images obtained in our preliminary studies have indicated that cells mostly tend to hug fibers, although some cells that adhere at fiber junctions will straddle different fibers. This will inevitably induce changes and additional stresses to the cytoskeleton, as there was a driving force towards stretching the cell membrane further in order to maximize cell-fiber contact. This intersection of T cell biology and biomechanics presents itself as a future

potential avenue of study, as full elucidation of this behavior and the underlying proteins involved may lead to new techniques for the advancement of T cell-based immunotherapy.

Functionalization of meshes with activating antibodies to CD3 and CD28 provided for the primary and secondary T cell activation signals, respectively, and allowed for subsequent cell proliferation and stimulation. This binding process was performed via direct adsorption in this preliminary model. As evidenced in our study, this led to antibody desorption across the three days of cell stimulation, although the protein desorption did not appear to induce overstimulation of cells in culture in subsequent days. To mitigate this however, a covalent linkage strategy, for example via the biotin-streptavidin route, will be a potential focus of future experiments as discussed in the future directions section.

In addition to the aforementioned safety concerns, the primary observed advantage in our mesh platform has been its ability to induce higher levels of cell proliferation while maintaining similar levels of cell activation and functionality. As evidenced by our expansion data, PDMS/PCL meshes demonstrated the ability to outperform the Dynabead® platform by upwards of 5.6 to 12.5 times more cells in healthy patients. This fact, coupled with the comparable levels of IFNγ secretion in $CD4^+$ cells, CD107b membrane expression on $CD8^+$ cells, and overall phenotype distribution, is of particular importance, as this implies that the production of large amounts of active cells from an even smaller starting number is possible with the mesh. This is critical for the success of *ex vivo* expansion, as this would ideally allow technicians to withdraw less blood from the patient in order to produce the same results, particularly in the case of patients with weakened immune systems. Such is the case with patients suffering from various chronic illnesses such as CLL, where the expansion of exhausted PD-1^{high} T cell populations has previously posed a challenge to the

Dynabead® platform. As our current experiments show that PDMS/PCL meshes can produce up to 8.5 to 18.3 times more cells in CLL patients than Dynabeads® while again retaining similar levels of activation, we strongly believe that our mesh holds significant promise for improving the landscape and clinical development of adoptive immunotherapy.

In order to more fully elucidate what rigidities the cell sees on the mesh, a second set of experiments was designed to focus on mesh rigidity measurements via AFM. Our fluorescence imaging data in this experiment indicated that upon interaction with the mesh, cells will either hug a single fiber or adhere to several fibers at a node. Cells in these configurations will thus apply forces both normal to the mesh and tangential to the mesh (traction forces). Although preliminary experiments on the former, involving seeding T cells onto micropillar arrays, have indicated that traction forces are on the order of 0.1 nN, this phenomenon remains not fully studied.

We therefore aimed to build off the work of Baker *et al* by probing the effects of different forces on microscale perceived rigidities and bending stiffness. While their work focused on PCL fibers via tangentially applied forces in AFM, ours focused on the use of PDMS/PCL hybrid fibers and probing forces normal to the fiber. Besides spanning a different range of rigidities, testing of PDMS/PCL fibers posed an additional challenge as our blended fibers have been observed to be more adhesive than PCL fibers. In other words, additional forces and phenomena stemming from intrinsic material properties as well as mesh geometry were necessary to be taken into account for this experiment. This was perpetuated by our initial findings via AFM that local rigidity values for experimental meshes ranged from approximately 640 kPa to 1.4 MPa, with additional increases in rigidity associated with aging of fibers. Given the relatively high cell expansion numbers achieved by experimental meshes, there was thus a discrepancy between these initial AFM-reported rigidity

values and our expected findings, namely, that rigidities would range in the tens to low hundreds of kPa. Our goal here was thus to construct a more accurate quantitative model for the perceived rigidity, termed E_{eff}, as experienced by the cell. Considerations in calculating bulk rigidities thus needed to be modified in order to construct such a model.

Analysis of mesh-adherent cells were conducted along the baselines of simple mechanics, starting with the fundamental theory of Euler and Bernoulli. For this analysis, we approximated the mesh fiber as a uniform cylindrical beam with fixed radius, calculated from SEM and AFM images. Due to force-dependent deformations in preliminary AFM scans, deformation δ was postulated to be comprised of both Hertzian and cantilever mechanics contributions, as opposed to purely Hertzian as with standard AFM models for rigidity calculation. That is, in lieu of a direct proportionality between δ and the square root of applied force, we postulated that deformation would be a sum of a linear and root component of applied force, in addition to a linear offset factor to account for experimental error.

Applied force was approximated as the peak force setpoint, or pFS, exerted by the AFM tip. In actuality, the total force experienced was not simply the pFS, but would include contributions from other factors such as materials adhesive forces, traction forces from fiber-fiber interactions, the weight of the cell pushing down on the fiber, etc. However, these factors were not taken into consideration in this model due to their negligible contributions. For example, previous reports by Phillips *et al* have indicated that an approximate mass for a T cell at rest (V = 230.9 ± 78.5 fL) as 18.7 ± 0.6 pg[39]. As the cell is in an aqueous environment during stimulation, factoring in the buoyancy force amounts to a very negligible additional force on the order of < 1 pN.

Approximation of average deformation $\bar{\delta}$ through analysis of the average distance from any node a point on a fiber resides via SEM scans, combined with material-specific curve fitting and the overall dominance of cantilever force contributions to the overall value of E_{eff} allowed us to formulate an equation for E_{eff} that was independent of force and only depended on mesh fiber geometries. This was of particular importance as it demonstrated that within forces in the nN range and similarly to the bulk material Young's modulus, E_{eff} is independent of applied force.

Note that $E \neq E_{eff}$, as the former refers to an intrinsic material property driven by the intermolecular forces of attraction of chemical structure of the material, while the latter is dependent upon the actual geometry of the material. Through this process, the values of E_{eff} for low [PDMS] and high [PDMS] meshes were estimated to be 294 and 251 kPa, respectively. While this much more closely matched expected values, it should be noted that the rigidities of these fibers did not differ significantly from each other. This would support the previous observation in specific aim 1b in the cell proliferation experiments: although both experimental meshes yielded significantly more doublings than with the Dynabeads® platform, the difference in maximum doublings between both meshes was not significant. If the cells were responding to perceived substrate rigidity, as was postulated, this similarity in rigidity would have manifested in a similar cellular response. The correlation between the significantly higher E_{eff} value for pure PCL meshes and the decreased number of doublings elicited further supports this conclusion: pure PCL meshes, which were estimated to have perceived rigidities of approximately 1.58 MPa, or about 5-6 times more rigid than PDMS/PCL meshes, yielded only 6 maximal doublings, compared to 9-10 maximal doublings for experimental meshes. This production of upwards of 8 to 16 times more cells on experimental meshes over rigid control meshes indicates that mechanosensing was indeed at play.

Note that protein adhesion was seen to desorb from experimental and control meshes at a similar rate during the cell activation phase of the experiment, thus indicating that differences in cellular response is driven by the material and material geometry, not by the antibody coating.

As cells predominantly felt cantilever forces on the mesh, an array of mesh fibers made of the same material were synthesized in order to attain values of E_{eff} on the range of 10^4 to 10^6 Pa as calculated by our constructed model. Correlation of the resulting expansion profiles with the study performed in 2012 by O'Connor *et al* revealed that mesh performance was on par with those on a planar surface in order of comparable rigidity. By comparing the cell proliferation and activation of a planar surface and a mesh surface of equal rigidity (or pseudo-rigidity), one can directly evaluate the effect of using a mesh as a culture substrate instead of a planar surface. Such information would hold significant promise in advancing the development of T cell-based adoptive immunotherapy for both research and clinical usage.

Future directions

Although the results from this series of experiments hold significant promise for furthering the advancement of ACT, this work also opens up multiple areas for future research from both a basic science as well as a materials and biomedical device engineering perspective.

One key evaluation criterion in the adaptation of an *ex vivo* stimulation platform for clinical use is its ability to produce sufficient numbers of cells, as well as compatibility with existing production mechanisms. Bench-scale expansion protocols, as presented in this thesis, have yielded promising results. However, larger-scale processes will have to be developed in order to fully realize this technology in the clinical setting. The Dynabead® platform is readily scalable: one easily can modulate the amount of beads added to a bioreactor system to accommodate higher starting populations. However, our PDMS/PCL mesh platform is less dense than water and thus floats without another substrate to weigh it down. Coating the inner surface of a bioreactor is one possibility, however, this is likely not feasible given the current electrospinning technology. One potential idea explored by our lab thus far is the use of PDMS/PCL meshes on printed three-dimensional polymeric scaffold inserts that can be mounted inside standard 50 mL centrifuge tubes. Preliminary models conducted by culturing cells on these mesh scaffolds have consisted of mounting centrifuge tubes onto a rotating platform, thus providing cells with slow, constant mixing, with manual oxygenation by opening up tubes every 12 h in a sterile incubator environment. Although cell populations cultured through this process have been observed to have comparable levels of activation to small-scale expansions, this process involves many manual steps and would not be viable for commercial processes. Therefore, there is a need for the development

of cell engineering devices and protocols to better incorporate the PDMS/PCL mesh platform into a more well-automated, scalable, bioreactor.

Current manifestations of the mesh platform have activating antibodies linked to the underlying mesh via direct adsorption. We have demonstrated that the dissociation of antibody from the mesh is relatively low, at approximately 70% antibody attachment upon separation of cells from the activating surface. However, this dissociation of antibody may lead to adverse patient reaction if left in the final cell transfusion, especially given the fact that the antibodies in question are general agonists for both the primary and secondary stimulation signals for naïve T cells. Therefore, there exists a need to further develop a method to covalently link activating antibody to the surface of the mesh. One possible and viable option is the use of a biotin / streptavidin linker and directly tether anti-CD3 and anti-CD28 molecules to the mesh without the intermediate use of the capture antibody as was done in this series of experiments. This would effectively decrease the cost of platform manufacturing as well as increase patient safety.

Other design parameters can be optimized as well: for example, although our platform was observed to significantly yield higher levels of cell division than the clinical gold standard, the use of mechanical pipetting utilized to harvest cells may have left cells stuck in the mesh matrix. It should be noted that while cells are seen to naturally detach from the mesh typically around day 4, cells were harvested at day 3 in order to keep protocols in line with the Dynabead® expansion protocol. Therefore, in order to increase the harvesting efficiency of stimulated T cells from the mesh, one could construct a degradable mesh, in which the addition of a compound would cause the fiber matrix to break down. Subsequent centrifugation and washing with media or buffer would allow for the separation of cells from broken down mesh fibers. This would be analogous

to the use of citrate, a chelating agent for calcium ions to break down alginate, a naturally occurring polysaccharide whose characteristic egg-box structure is stabilized by calcium ions. The use of alginate may not be of optimal usage in the context of T cell immunotherapy due to the concentrations of calcium released by the degradation of the alginate structure and the potential fragility of patient cell populations. However, other materials with similar degradation properties and low rigidities may have use in the context of the engineering of the mesh platform.

An additional design parameter of note is the inclusion of PCL in the electrospinning feed. As previously discussed, PCL was utilized in the electrospinning of our PDMS-based meshes in order to serve as a viscosity modulator. Notably, PCL is biocompatible, non-cytotoxic, and readily commercially available. Ideally however, this mesh platform would be synthesized out of pure PDMS, or PDMS and a softer, biocompatible material, in order to achieve lower rigidities. One potential workaround is the use of a hydrogel system instead of an electrospun mesh system, but with pore sizes similar to ones on PDMS/PCL meshes from this series of experiments. This could potentially allow for even higher levels of cell activation and proliferation through the presentation of softer surfaces while retaining the high surface area to volume ratio and other desirable properties of the mesh.

Furthermore, studies performed thus far have focused on the activation and proliferation of conventional, $CD4^+$ and $CD8^+$ T cells. While the expansion of these cell types will undoubtedly be useful for the treatment of a wide range of chronic illnesses in which the patient's immune system is unable to successfully restore homeostasis, these cell types will not be as effective for the treatment of autoimmune diseases. In these diseases, such as type II diabetes, inflammatory bowel disease (IBD) and rheumatoid arthritis, the promotion of regulatory T cells may prove useful

in suppressing an overactive immune system. As regulatory T cells are notably different than conventional $CD4^+$ and $CD8^+$ T cells in surface marker expression and behavior, further research may prove useful in optimizing mesh design parameters for these applications.

While the expansion of CLL patient-derived T cells showed strong indication that our softer substrates can invoke higher levels of cell activation and proliferation than the clinical gold standard, the high degree of patient to patient to variability, even in the same Rai stage, alludes to other variables than Rai stage at play in terms of indicating whether or not a patient's cells were suitable for expansion. This is not of particular surprise, as the Rai stage of a patient only refers to the enlargement of the spleen, lymph nodes, or lack of certain cell types, not particular characteristics of the mutated B cells themselves. One possible hypothesis for this variance lies in the genetic mutation rate of the variable region of the B cell receptor (BCR) heavy chain (V_H). Intriguingly, studies conducted by Stilgenbauer *et al.* have suggested that higher levels of V_H homologies at mutations sites on chromosomes 11, 12, and 17 correlate to a decrease in patient survivability[27]. As demonstrated in figures 2 and 3 of their paper, the estimated average survivability for patients with V_H homologies $\geq$ 97% in these regions is approximately 79 months' post diagnosis, compared to over 192 months for patients with higher levels of genetic mutation. Although the exact mechanism for this has not been fully explored yet, this phenomenon may have implications for determining which CLL patients' cells would be suitable for adoptive immunotherapeutic expansions. Additionally, work by Damle *et al* has indicated that the expression of surface marker CD38 may be another potential indicator for cell survivability, and perhaps ease of cellular expansion[38]. In their analysis, Damle *et al* showed that patients with a higher expression rate of $CD38^+$ mutated B cells (defined as 30% or more) had a higher percentage

of B cells with mutated V_H homologies. As such, future experiments may focus on the expansion of cells from patients with different V_H homologies and/or expression levels of CD38 of over 30%, but with the same Rai stage.

AFM studies conducted in this series of experiments have been done with the overall goal of elucidating what rigidities a T cell experiences upon coming in contact with the mesh. However, the microscale geometries characteristic of the mesh and indentation forces from the AFM tip do not lend themselves well to any commonly used models for AFM-based rigidity calculation. The reasons behind this are clear: besides the fact that microscale fibers do not resemble semi-infinite planes, observations thus far have indicated that the observed rigidity of the mesh appears to be a quadratic function in the maximal applied force, or pFS. Additionally, substrate deformation also appears to vary with pFS; this is in direct deviation with the standard AFM models for rigidity, specifically the Sneddon and DMT rigidity models, as substrate deformation is assumed to be zero or negligible in both cases. Ideally, the pFS would be equal to the force exerted by a T cell on the mesh; however, this information has yet to be fully studied.

Additionally, our quantitative model has notably omitted the contributions from a wide range of other factors that may affect E_{eff} such as fiber-fiber traction forces, tip adhesion forces, and peak force error. Although these forces were not considered significant for the purposes of this model due to their hypothesized low contribution to the E_{eff} as a whole, a more in-depth model can be constructed to account for these factors. This would likely involve a re-derivation of Euler-Bernoulli theory and the calculation of deformation with respect to characteristic fiber length scale. Also due to the dual material composition of our PDMS/PCL meshes, tip adhesion forces need to be considered carefully as while PDMS is a relatively adhesive material, PCL is much less so. The notion

of persistence length was also omitted from this experiment due to the short length scales associated with inter-nodal fiber distances. However, for meshes composed of longer fibers, such as mesh formulation E from the model verification experiments, the notion of persistence length may come into play.

Furthermore, many of the fundamental assumptions from Euler-Bernoulli theory were held constant throughout the derivation of this model, such as a uniform cross-sectional area and uniform shear modulus, may in fact not hold true with these meshes. As observed in SEM micrographs and AFM topological scans, fibers are not perfect circular cylinders, but may be best modeled as cylinders with elliptical cross sections: fibers tend to be flattened slightly parallel to the plane of the collection electrode and are stacked on top of underlying mesh fibers. Likewise, shear moduli of meshes, which was not considered for the purposes of this model, may come into consideration due to how the cell interacts with the mesh. Focal adhesions between a T cell and a mesh fiber will result in not just a force normal to the direction of the fiber, but a pulling force tangential to this direction as well. Such a pulling force will contribute to fiber deformation, and will thus require consideration of the shear modulus of the fiber. However, the strength of such forces has not yet been fully studied as of this writing.

One final point of discussion about the utility of our derived model is that verification of this model has only been tested with our PDMS/PCL mesh system. As research towards development of an improved platform for T cell-based ACT continues to evolve, new materials and fabrication techniques may be developed. As a result, this model may not be fully accurate for other mesh systems: testing with other materials and mesh compositions may be necessary to further develop this model to yield a more unifying equation for E_{eff} in fibrous meshes.

As the average lifespan increases and the prevalence of chronic illnesses, including but not limited to cancer, increases in turn, the demand for immunotherapeutic technologies will rise as well. As the results from this series of experiments open up a multitude of new avenues of research, it is with great likelihood that further development of realization of ACT will be perpetuated by the continuation of this research. Be it in the modification of design parameters to improve mesh performance, the engineering of improved methods for scalability and clinical adaptation, or the development of a more rigorous model for E_{eff}, the avenues of research opened up by this series of experiments will be invaluable to the development of adoptive immunotherapy and biomaterials research as a whole.

References

- [1] Siegel R, *et al*. CA Cancer J Clin 2018:68(1) 7–30
- [2] American Society of Clinical Oncology. Journal of Oncology Practice. 2014:10(6) 1-25
- [3] Restifo N, Dudley M, and Rosenberg S. Nature Reviews Immunology. 2012:12 269-281
- [4] Brentjens R, et al. "Driving CAR T cells forward." Nat Rev Clin Oncol. 2016 13, 370–383
- [5] Rosenberg S, Resfito N, Yang J, Morgan R, and Dudley M. Nature Reviews Cancer. 2008:8 299-308
- [6] Rosenberg S, Packard B, *et al.* New England Journal of Medicine. 1988:319 1676-1680
- [7] Gill S, Tasian S, Ruella M, *et al.* Blood. 2014:123(15)
- [8] Thara E, Dorff T, Pinski J, and Quinn D. Maturitas. 2011:69 296-303
- [9] Patel D. *Separating Cells*. Oxford: BIOS. 2001
- [10] Neurauter A, *et al.* Advances in Biochemical Engineering and Biotechnology. 2007:106 41-73
- [11] Judokusumo E *et al*. Biophysics Journal. 2012:102(2) L2-L5
- [12] Haycock J. *3D cell culture methods and protocols.* New York: Humana Press. 2011
- [13] Janeway C. *Immunobiology: The immune system in health and disease* (6th edition). New York: Garland Science. 2005
- [14] Kindt T, and Goldsby R. *Kuby immunology* (6th edition). New York: WH Freeman. 2007
- [15] Persano L, Camposeo A, Tekmen C, and Pisignano D. Macromolecular Materials and Engineering. 2013:298(1) 504-520
- [16] Zhang CL and Yu SH. Chemical Society Reviews. 2014:43(2) 4423-4448
- [17] Schwartz M. Cold Spring Harbor Perspectives in Biology. 2010:2(12)

- [18] O'Connor RS, *et al*. Journal of Immunology. 2012:189(3) 1330-1339
- [19] Horejs C-M. Nature Reviews Materials. 2017:2(17067)
- [20] Niu H, Wang H, Zhou H, and Lin T. RSC Advances. 2014:4 11782-11787
- [21] Yang D *et al*. Biomacromolecules. 2009:10 3335-3340
- [22] Ratner B, Hoffman A., Schoen F, and Lemons J. *Biomaterials Science, Third Edition*. Wiley. 2013
- [23] Raab M, *et al*. Nature Communications. 2017:8(16001)
- [24] Roa J., *et al*. Calculation of Young's Modulus by Means of AFM. Recent Patents on Nanotechnology 2011:5 27-36
- [25] Gere J. *Mechanics of Materials, Sixth Edition*. Thomson. 2004
- [26] Sanz-Ramos P, Mora G *et al*. Osteoarthritis and Cartilage. 2012:20(8) 931-939
- [27] Rosenberg S, *et al*. Nat Rev Cancer. 2008: 8(4) 299-308
- [28] Luo T, Mohan K, Iglesias P, and Robinson D. Nature Materials. 2013:12 1064-1071
- [29] Li W, Cato T, *et al*. Journal of Biomedical Materials Research. 2002:60(4)
- [30] Liu C, Zhu C, *et al*. Bone Research. 2015:3(15012)
- [31] Baker S, *et al*. Materials Science and Engineering C. 2016:59. 203-212
- [32] Park S and Gao X. Journal of Micromechanics and Microengineering. 2006:16 2355-2359
- [33] Bauchau O.A., Craig J.I. *Euler-Bernoulli beam theory*. Solid Mechanics and Its Applications, vol 163. Springer, 2009
- [34] Asay D, Hsiao E, and Kim S. Review of Scientific Instruments. 2009:80(6)
- [35] Lee J, Park C, and Whitesides G. Anal. Chem. 2013:75 6544-6554
- [36] Stilgenbauer S, *et al*. Leukemia. 2002:2(16) 993-1007

- [37] Jiang Y, and Turner K. Extreme Mechanics Letters. 2016:9 119-126
- [38] Damle *et al.* Blood. 2007:110(9) 3352-3359
- [39] Phillips K., *et al.* Frontiers in Oncology. 2012:2(72)